MAY 19 2004

QC
851
.F5
no.
2004-03

On the Hurricane Intensity Issue

T. N. Krishnamurti, S. Pattnaik, L. Stefanova,

aya Kumar, B. P. Mackey, A. J. O'Shay and Richard J. Pasch[1]

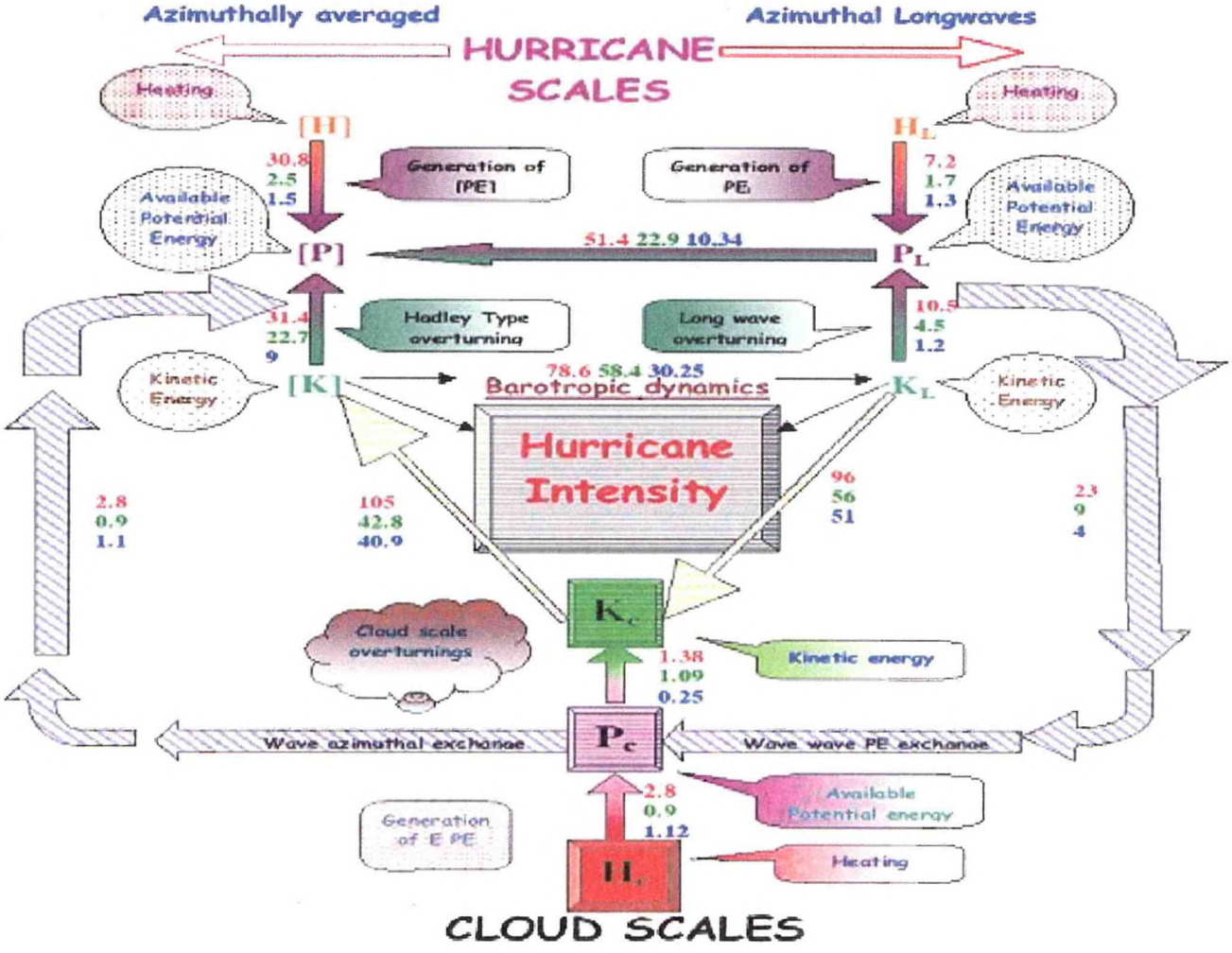

Department of Meteorology
Florida State University
Tallahassee, FL 32306-4520

[1]TPC, National Hurricane Center,
NOAA/NWS, Miami, FL 33165-2149

Supported by:
NSF ATM-0108741
NASA NAG5-9662
NASA NAG8-1848
FSURF 1338-895-45

FSU Report No. 04-03
April 2004

MAY 19 2004

S

On the Hurricane Intensity Issue

T. N. Krishnamurti, S. Pattnaik, L. Stefanova,
T.S.V. Vijaya Kumar, B. P. Mackey, A. J. O'Shay

Department of Meteorology
Florida State University
Tallahassee, FL 32306-4520.

and **Richard J. Pasch**

Tropical Prediction Center, National Hurricane Center,
NOAA/NWS, Miami, FL 33165-2149, USA

LIBRARY

MAY 04 2006

National Oceanic &
Atmospheric Administration
U.S. Dept. of Commerce

QC
851
.F5
no.2004-03

April 2004

NOAA Science Center
Betty Petersen Memorial Library
World Weather Bldg., Room 103
5200 Auth Road
Camp Springs, MD 20746

Abstract

The intensity issue of hurricanes is addressed in this paper using the angular momentum budget of a hurricane in a storm relative cylindrical coordinates, and a scale interaction approach. In the angular momentum budget in storm relative coordinates, a large outer angular momentum of the hurricane is depleted continually along inflowing trajectories. This depletion occurs via surface and planetary boundary layer friction, model diffusion, and 'cloud torques', the latter is a principal contributor to the diminution of outer angular momentum. The eventual angular momentum of the parcel near the storm center determines its final intensity. The scale interaction approach is the familiar energetics in the wave number domain where the eddy and zonal kinetic energy on the hurricane scale offer some insights on its intensity. Here, however, these are cast in a storm centered local cylindrical coordinate as a point of reference. The wave numbers include azimuthally averaged wave number 0, principal hurricane scale asymmetries (wave numbers 1 and 2, determined from data sets) and other scales. The main questions asked here relates to the role of the individual cloud scales in supplying energy to the scales of the hurricane, thus contributing to its intensity. A principal finding is that cloud scales carry most of their variance, via organized convection, directly on the scales of the hurricane. The generation of available potential energy and the transformation of eddy kinetic energy from the cloud scale are in fact directly passed on to the hurricane scale by the vertical overturning processes on the hurricane scale. Less of the kinetic energy is generated on the scales of individual clouds that are of the order of a few km. The other major components of the energetics are the kinetic to kinetic energy exchange and potential-to-potential energy exchange among different scales. These occur via triad interaction and were noted to be essentially downscale transfer, i.e., a cascading process. It is the balance among these processes that seem to dictate the final intensity.

1. Introduction

In this paper we explore two avenues for the hurricane intensity issue. Both of these are diagnostic approaches and are applied here to the data sets derived from a very high-resolution forecast model. A somewhat reasonable hurricane intensity forecast from a high-resolution model was necessary in order to portray the workings of the proposed diagnostic frameworks. The two approaches portrayed here can be labeled the angular momentum based diagnosis of hurricane intensity and a scale interaction based diagnosis of the storm's energetics. In the former approach, a reservoir of high angular momentum air from the outer reaches of the hurricane has a large control on its intensity. That outer angular momentum is affected by the torques the parcels experience as they move towards the high intensity region. The latter approach asks about implications of the cloud scales on the eventual energy (that indirectly relates to the intensity) of a hurricane.

The initial data sets for this study came from the ECMWF operational analysis plus dropwindsonde data sets from research aircraft and satellite data. A list of acronyms appears in Table 1. Furthermore, this study is based on a somewhat realistic simulation of a hurricane (Hurricane Bonnie of 1998) that was generated using a non-hydrostatic microphysical meso-scale model (the MM5). The model output data sets were used here to carry out the diagnostic enquiries.

This study became possible due to two recent advancements in data and modeling. CAMEX-3 and CAMEX-4 are recent field experiments where joint data initiatives of NASA, NOAA and the U.S. Air force provided an extensive coverage of observations. They deployed as many as six research aircraft for the surveillance of hurricanes on a daily basis. These research aircrafts provided as many as a total of 100 dropsondes per day covering profiling data

for winds, temperature, humidity and pressure. In addition to these, a NASA aircraft provided specialized moisture profiles from an instrument called LASE. Another major data set was a ½ degree latitude/longitude operational analysis data of ECMWF. Using these data sets, we performed variational data assimilation, Rizvi et al. (2002) and Kamineni et al. (2003, 2004), to analyze the CAMEX storms of the years 1998 and 2001. This mix of data sets provides a unique coverage of observations for hurricane modeling.

In the modeling area, it is now possible to carry out high-resolution simulation with meso-scale non-hydrostatic microphysical models. Numerous recent applications with the NCAR MM5 model have shown the possibility for such simulation. Braun (2002) analyzed the storm structure and eye-wall buoyancy of Hurricane Bob using a multiply nested MM5 model with moving nest capability and demonstrated reasonable distributions of vertical motion in the eyewall. Similar studies were carried out by different research groups to resolve the cloud-scale features of hurricanes using MM5 model, e.g., Bao et al. (2000), Braun and Tao, (2000), Chen and Yau, (2001), Davis and Bosart, (2001), Davis and Trier, (2002), Zhang et al. (2003), and Liu et al. (1999). A multiple nested model with an inner resolution of 1 km provides the possibility for asking questions on the role of model's deep convection on the intensity issue of hurricanes.

In his seminal paper on atmospheric energetics in the wave number domain, Saltzman (1957, 1970) laid the foundations for studies of scale interactions. Exploring the energy exchange among waves and waves, and waves and zonal flows, he portrayed the mechanism for the driving of the middle latitude zonal flows (i.e., the zonally averaged jets) in the atmosphere. That framework was in spherical coordinates. For studies of a hurricane it is relatively straightforward to cast this system on to a polar coordinate system, details of which are provided in Appendix 1. This transformation provides information on the kinetic and potential energy

exchange among the azimuthally average flows and other azimuthal waves. The cloud (convection) scale being much smaller than that of the hurricane, the mode of communication of information from the cloud scale to the hurricane scale was not clearly apparent. The scale of convection (updrafts and adjacent downdrafts) is of the order of a few kilometers whereas the scale of hurricane is of the order of several hundreds of kilometers. Clearly an issue of scale interaction needs exploring in this context. A budget of kinetic energy for the scales of the hurricane can be revealing on its intensity. The angular momentum perspective starts with a large reservoir of high angular momentum air at large radii. That air is generally brought into the storms interior along inflow channels of the lower troposphere. That large angular momentum (following parcel motion) is depleted by the surface and internal friction torques (cloud torques) and by the pressure torques. The parcel arrives at inner radii where the storm intensity (the maximum wind of the hurricane) is explicitly determined from the value of the angular momentum the parcel arrives with. This paper attempts to provide some insight on these two different approaches for the understanding of hurricane intensity.

2. Observational Aspects:

Hurricane Bonnie started out as a tropical depression to the east of Antilles near 50^{o} W and 15^{o} N on August 19, 1998 around 1200 UTC, slowly moving in a northwesterly direction as shown in Fig. 1. The tropical storm stage was reached on August 20 at 2000 UTC, and the hurricane force winds were first noted on August 22 at 0000 UTC. This hurricane made a recurvature near the North Carolina coast and weakened to tropical storm force winds at 1800 UTC on August 27, 1998. This storm was most intensely monitored by hurricane reconnaissance aircraft. Our study covers a 72-hour period between 22 and 25 August 1998. During this period, Hurricane Bonnie's maximum winds varied between 33.5 to 51.5 ms^{-1}. The satellite visible

imagery during this period (Fig. 2) showed a well-defined storm with active banding to its south. However, after recurvature and a merger with a front, the cloud cover was elongated northeastwards. The storm imagery appears similar to that seen in many Category 3 storms of the Atlantic basin, here the maximum winds were close to 115 mph (51.5 ms^{-1}). We shall not describe the detailed structure of Hurricane Bonnie here since this is a well-studied storm, and is described in some detail by Pasch et al. (2001) in their seasonal summary and our laboratory; Rizvi et al. (2002).

The data sets for this study came from diverse sources: ECMWF, CAMEX-3 and satellite data sets. The initial state and boundary conditions for this modeling study was prepared using the following data sets: (i) Operational real-time ECMWF'S analyzed data files (provided at 0.5 degrees lat/long grid and 28 vertical levels.

1) Six research aircrafts provided dropsonde and special moisture profiling data sets (the LASE instrument). There was mid tropospheric surveillance from two NOAA P3 aircraft, a NOAA G4 near the tropopause level, a NASA P3 aircraft, a NASA DC8 (flying near the 250 hPa level), and a NASA ER2 flying near 60,000 feet in the lower stratosphere. These data sets were analyzed using our FSU variational data assimilation (3DVAR) following Rizvi et al. (2002) and Kamineni et al. (2003, 2004) where the hurricane forecast impacts from these additional observations of the CAMEX field campaign were addressed. This analysis was carried out on a spectral resolution of T170 (transform grid separation near 70 km).
2) These data sets were next subjected to physical initialization (i.e., rain rate initialization) following Krishnamurti et al. (1991, 2001) Here rain rate estimates were derived from the Microwave Instruments on board TRMM and three DMSP satellites.

3) These analyzed data sets were simply interpolated using bi-cubic splines on to a variable grid resolution of the MM5 model used in this study.

a. The NCAR-PSU MM5 Model

The numerical simulation of Hurricane Bonnie (1998) was carried out using the Pennsylvania State University-National center for Atmospheric research (PSU-NCAR) non-hydrostatic fifth-generation Mesoscale Model (version 3.6). A 72-hr simulation of Hurricane Bonnie (0000 UTC 22 August – 0000 UTC 25 August 1998) was carried out using a variable resolution nesting configuration. Here we use four domains (Fig. 1) with a horizontal grid spacing of 27, 9, 3 and 1 km and having domain size of 98x94, 186x222, 369x444, 501x501 grid points respectively. These grid meshes include 23 vertical half sigma (σ) levels. The 27 km and 9 km domains are one-way nested whereas the 3 km and 1 km nests are two-way nested. The physics options used for the coarser grids at 27 km and 9 km included the Betts Miller cumulus parameterization (Betts and Miller 1986, 1993), a simple ice explicit scale cloud microphysics scheme (Dudhia, 1989), the MRF planetary boundary scheme (Hong and Pan, 1996), and a cloud radiative scheme of Dudhia (1989). The physics options for the 3 km and 1 km grids were similar to the coarse grid simulations except that no cumulus parameterization scheme was deployed, and convection was explicitly handled.

The combined 6-aircraft CAMEX flights for the surveillance of an entire storm were only conducted on a few successive days. Thus it was not possible to validate in detail the performance of the MM5 model. However, the simulated details, at the high-resolution, were sufficiently realistic in terms of structure, motion and intensity to carry out the main objectives of this study, which are the angular momentum and the scale interaction perspectives. The observed maximum reported winds from the National Hurricane Center for days 1, 2 and 3 of

this study were 46, 51 and 51 ms^{-1} and the corresponding model predicted maximum winds at 850 hPa level were around 27, 35 and 45 ms^{-1} respectively. The central pressure comparisons were: observed estimates 962, 954 and 963 hPa and the model predicted values were 1002, 996 and 984 hPa. The observed and predicted tracks of Hurricane Bonnie were illustrated in Fig. 1. There are clearly some track errors but that was not a primary issue here. It is our experience that ensemble averaging of tracks from multimodels appears to generally do better than single models, Krishnamurti et al. (2000), Williford et al. (2003). Some of the initial state fields are illustrated in Figs. 3 a,b,c. The sea level pressure on August 22, 1998 at 0000 UTC, shown in Fig. 3a, depicts a low-pressure system to the southeast of the regional model domain. The central pressure at this time was around 1006 hPa and the maximum winds were 24 ms^{-1}. Strong pressure gradient to the north was indicative of the strong trades. The scale of this closed low-pressure field extended from 71 ^{o}W to 65 ^{o}W. The tangential wind maxima (Fig. 3b) at the initial time were around 24 ms^{-1} to the north of the storm and were of the order of 13 ms^{-1} to the south of the storm. The weakest winds are located over the storm center. The field of total angular momentum (in a storm relative frame of reference) is illustrated in Fig. 3c. As to be expected, the angular momentum increases at increasing radius. Values near the storm's center are around 0.2×10^{-7} m^2s^{-1} and increase to around 16×10^{-7} m^2s^{-1} towards the northwest of this domain. Larger values at increasing radius south of the storm are not covered in this illustration.

Figures 4 a,b,c show the streamline isotachs at the 850 hPa level from the forecasts of the meso-scale model at the end of days 1, 2 and 3. The northwestward motion of the storm is reasonably captured by the forecast. An interesting and prominent feature is the evolution of an asymptote of convergence to the south (by day 3 of forecast, Fig. 4c). This feature, in storm relative coordinates, was an important inflow channel for Hurricane Bonnie.

3. The angular momentum approach on the interpretation of hurricane intensity

The angular momentum perspective starts with a large reservoir of high angular momentum air at the large radii. That air is generally being brought into the storm's interior mainly along inflow channels of the lower troposphere. That large angular momentum (following parcel motions) is depleted by the surface and internal frictional torques, by pressure torques, and by cloud torques. The parcel arrives at the inner radii where the storm intensity (the maximum wind of the hurricane) is determined by the value of the angular momentum the parcel arrives with at that location. This could be called an outer thrust that seemingly determines the hurricane's intensity. The weakness of this argument is that the inflow channel is assumed to be a prescribed entity here. One can ask how did that come about? An inner thrust, a second perspective, calls for a detailed knowledge of the storm clouds. Knowing better microphysics, we can perhaps model these clouds better, and these clouds may be the ones that carve out the inflow channels in the first place. The angular momentum story could well be a consequence of a systematic and organized cloud growth. Clearly, carefully designed numerical experiments are needed to sort out these outer and inner thrust issues in their correct perspectives for addressing the sensitivity of hurricane intensity to various parameters. Most likely, these issues are inter-coupled.

For the distribution of angular momentum in storm relative coordinates, we map the field of $M = V_\theta r + fr^2/2$. The total angular momentum at the 850 hPa level (Fig. 3b) is larger at increasing 'r', i.e., away from the storm center. At large radii, $fr^2/2$ exceeds $V_\theta r$ and this distribution of angular momentum at outer radii looks almost the same for most storms.

The angular momentum equation is defined by multiplying the tangential equation of motion by the radial distance r (from the storms center):

$$\frac{dM}{dt} = F_\theta r - \frac{1}{\rho}\frac{\partial \rho}{\partial \theta}; \quad \text{where} \frac{d}{dt} \equiv (\mathbf{V} - \mathbf{C}) \bullet \nabla \tag{1}$$

$\frac{dM}{dt}$, the change in angular momentum, is calculated in a storm relative frame of reference ($\mathbf{C}$ denotes the storm motion vector) and $F_\theta r$ is the frictional torque and $\frac{1}{\rho}\frac{\partial \rho}{\partial \theta}$ denotes the pressure torque. The change in angular momentum from pressure torques is given by:

$$\frac{dM}{dt} = -\frac{1}{\rho}\frac{\partial p}{\partial \theta} \tag{2}$$

or the corresponding tangential velocity change is given by

$$\frac{dV_\theta}{dt} = -\frac{V_\theta V_r}{r} - \frac{1}{\rho}\frac{\partial p}{\partial \theta} \tag{3}$$

The intensity change from pressure torques can be expressed by:

$$\frac{dV_\theta}{dt} = -\frac{V_\theta V_r}{r} - \frac{1}{r}\frac{1}{\rho}\frac{\partial p}{\partial \theta} \tag{4}$$

This contribution to intensity changes arising from the pressure torques can be estimated following three dimensional parcel trajectories. Once the change in $V_\theta r + fr^2/2$ contributed by torques is known, then it is easy to compute the change in the intensity V_θ following segments of parcel motions that arise from effects of each type of torques. Specifically we can tailor such a budget to the maximum intensity of the storm. This is further discussed in Section 5 of this paper.

One of the well-known pressure asymmetry in hurricanes arises from the so-called 'Beta Gyres'. If the symmetric part of the pressure field of a hurricane is removed from its total pressure field, then one can visualize these beta gyre structures. The structure generally contains higher pressures to the right of the storm's center and lower pressure to its left. Figure 5 illustrates this structure for hurricane Bonnie for the sea level pressure from day 3 of forecast.

The presence of a beta gyre implies the presence of pressure torques. This is usually on rather larger scales, i.e. azimuthal wave numbers 1 and 2 and the amplitude of this torque is rather small. Another contributor to pressure torque comes from the deep convective elements (simulated by the high resolution model) that carry pressure perturbations. With vertical motions of the order of one to 10 ms^{-1}, small-scale pressure perturbations of the order of a few hPa on the scale of these deep convective elements abound in the predicted pressure fields. Because of the smaller horizontal scales of these convective elements, these perturbations can convey robust local pressure torques. However, on either side of these pressure perturbations, opposite signs of the azimuthal pressure gradients are found, thus the increase and decrease of angular momentum essentially cancel along segments of inflowing trajectories from these pressure perturbations.

a) Frictional Torques

In the version of the MM5 that is used in our study, the surface fluxes of momentum are defined via a Bulk Aerodynamic Formula, Deardorff (1972) and Grell et al. (1995). Here the constant flux layer is 86 meters deep. The disposition of surface fluxes above the constant flux layer within a PBL follows the MRF PBL scheme that was based on the work of Hong and Pan (1996). This is a non-local scheme that permits counter gradient fluxes of moisture by large scale eddies. The eddy diffusivity coefficient for momentum is a function of the friction velocity u* and the PBL height is a function of a critical Bulk Richardson number. The vertical disposition of these sub grid scale surface momentum fluxes are carried out using the K- theory. The profiles of implied sub grid eddy momentum fluxes determine the vertical distribution of surface fluxes. The frictional torques, $F_\theta r$, do have vertical distributions. They largely mimic the surface torques through several vertical levels.

The outputs of the vertical fluxes of momentum between the surface level and the top of the PBL were stored for each hour of the forecast. In addition to these, the MM5 includes parameterization for the sub grid scale vertical diffusion of momentum that was also retrieved and stored. The resolved vertical fluxes of momentum by shallow and deep convection were explicitly calculated from the fields of u, v, and w. These were also stored at intervals of one hour. These provided a complete inventory of the momentum fluxes at surface, the PBL and the rest of the model column. The large outer angular momentum of inflowing air is constantly eroded by the frictional torques. This field varies from hurricane to hurricane largely due to different distribution of wind speeds, storm size and from the dependence of the diffusive exchange coefficients as a function of height and the Richardson Number.

b) Cloud Torques

Along segments of parcel trajectories, active cloud elements contribute to sizeable torques - we have designated these as cloud torques. The cloud torques appear to be a major contributor to the modification of angular momentum of inflowing parcel segments where model clouds were present. In the x-y-z frame of reference, cloud torques can be expressed by

$$\frac{dM}{dt} = -r\frac{\partial}{\partial z}\overline{W'V'_\theta} \qquad (5)$$

(here we are disregarding the horizontal eddy fluxes). Along the inflowing trajectory we identify a segment traversed by the parcel in a time Δt (across significant cloud element). The corresponding change of angular momentum across that segment is

$$\Delta M = -r\frac{\partial}{\partial z}\overline{W'V'_\theta}\Delta t \qquad (6)$$

The over bar on the right hand side denotes an average value across model simulated cloud elements within a trajectory segment. A net vertical divergence of eddy flux of momentum

$+\frac{\partial}{\partial z}\overline{W'V'_\theta}$ results in a net diminution of angular momentum. This is consistent with the increase of resolvable eddy flux $\overline{W'V'_\theta}$ as we go up from the ocean surface. The outer angular momentum is constantly being drained to the upper levels by the cloud turbulence. These results are presented in Section 5.

If a model forecast provides reasonable storm intensity, then it is possible to carry out an intensity budget using the angular momentum principle as a frame of reference.

4. The Scale Interaction Perspective

The hurricane's scale can be described by a few azimuthal wave numbers (e.g. wave number 0, 1, 2) that was noted in our analysis of the rainwater mixing ratio and Krishnamurti and Sheng (1985a,b). The field of rainwater mixing ratio in these high-resolution forecasts carries the signature of individual deep convective cloud elements. Figures 6 a,b illustrate the predicted rainwater mixing ratio at the 850 hPa level for days 2 and 3 of forecast. An azimuthal spectral analysis of these fields shows that a sizeable portion of the variance of the rainwater mixing ratio is accounted for by the first few harmonics. In Figs. 7a,b we show the power spectra of the rainwater mixing ratio for the initial time (shown as t=1) and at hour 24 (shown as t=2). The results for radii 0-40 km, 40-200 km and 200-380 km are presented here. At radii less than 200 km, considerable amount of the power resides in these low wave numbers. At the outer radii (200-380 km) the distribution shifts to smaller scales. The same result emerges when we examine the azimuthal spectra of the tangential velocity. The larger scales of the rainwater mixing ratio spectra are a clear reflection of the organization of convection. It thus appeared reasonable to designate wave numbers 0, 1, and 2 as the hurricane scales. On the other hand, the scales of the individual deep convective clouds appear to reside around the azimuthal wave numbers 20 to 30. Following Saltzman (1957, 1970), it is of interest here to explore the

interactions between the hurricane and the cloud scales. These interactions can be broadly described by (a) Available Potential to Eddy Kinetic; (b) Eddy Kinetic to Eddy Kinetic; and (c) Available Potential to Available Potential. In somewhat further detail, the following are twelve salient and grouped energy exchange components that comprise the total system. (Appendix 1 includes the mathematical details).

i) $<P_o \cdot K_o>$ is the conversion of azimuthally averaged (subscript *o*) potential energy (*P*) to the azimuthally averaged kinetic energy (*K*). This is a mechanism for the maintenance of hurricane intensity. This is akin to warm air rising and relatively colder air sinking from the Hadley type vertical overturning. In our hurricane domain, which encloses the entire troposphere below 100 hPa and the entire atmosphere within r $\leq$ 500 km, the rising of warmer air occurs near the eye wall clouds and the rain bands. The sinking of relatively cooler air occurs outside of the rain band and inside of the eye wall.

ii) $< P_l . K_l >$ denotes long wave (subscript *l*) vertical over turnings on the salient asymmetric scale of the hurricane such as azimuthal wave numbers 1 and 2. Since this overturning arises from a quadratic nonlinearity among vertical velocity and temperature on the individual long wave scales, this can only contribute to an in-scale energy exchange, i.e., available potential energy of wave number 1 can only generate eddy kinetic energy for wave number 1, the same being true for wave number 2. These overturnings generate eddy kinetic energy, thus contributing to an asymmetric velocity maximum. These waves generally exhibit phase locking, thus normally adding up to a single velocity maximum describing the principal hurricane asymmetry. It is relevant to make a note on the eye wall convection here. There has been much discussion on eye wall convection and its possible impact on hurricane intensity (Braun, 2002). Along a circular eye wall, if several tall cumulonimbus clouds are

located along its circular geometry, then the possibility clearly exists for the clouds to directly impact wave number zero. The azimuthally averaged heating along the eye wall would generate azimuthally averaged potential energy. That can be directly converted to azimuthally averaged kinetic energy (on the scale of wave number 0) from the vertical overturnings (ascend along the eye wall and descend inside and outside of the eye wall). Here we can see a direct role of organized clouds amplifying the hurricane intensity. Furthermore, local variations of deep convection along the eye wall can also produce local asymmetry in vertical circulations, local generation of available potential energy and local conversion to eddy kinetic energy for higher wave numbers such as 1, 2, and 3. Thus, local enhancement of intensity can also arise from the presence of organized local manifestation of the cloud scale vertical overturnings (akin to local Hadley type overturning).

iii) $<P_c \cdot K_c>$ is the contribution from the smaller scale (cloud scale – subscript *c*) overturning. This can only produce eddy kinetic energy on the same scales because of the previously stated quadratic nonlinearity $-\sum_i \frac{\omega_{ci} T_{ci}}{p}$. ω is the vertical velocity and T is the temperature at those scales.

iv) $\langle H_o \cdot P_o \rangle$ is the generation of available potential energy from heating, also arises from a quadratic nonlinearity (i.e. the product of heating and temperature) and as such this can only generate potential energy on the scale of that heating. The azimuthally averaged (wave number 0) heating generates available potential energy only on this scale.

v) $\langle H_l \cdot P_l \rangle$ is an in-scale generation of potential energy from the long wave scales of heating.

vi) $\langle H_c \cdot P_c \rangle$ is the smaller scale heating and can only generate available potential energy on the same (smaller) scales.

vii) $\langle P_s \cdot P_l \rangle$ is the nonlinear exchange of available potential energy from waves to waves. The available potential to available potential is a triad interaction among waves that satisfy certain trigonometric selection rules. Here, the possibility exists for smaller cloud scale (a pair of waves) to transfer potential energy to another azimuthal wave or vice versa. Once such a transfer occurs, then the 'in-scale vertical overturning' can in principle transfer the potential energy of azimuthal waves to the kinetic energy of that scale. This in turn can in principle indirectly contribute to the intensity of the hurricane. In these triple product nonlinearities, energy exchanges are dictated by selection rules. If three scales *m*, *n*, and *p* interact, then *p* has to be equal to *m+n*, *m-n* or *n-m* in order for a non-vanishing exchange to occur. This is the basis for triad interactions (Krishnamurti et al. 2003). This calls for two scales interacting with a third scale resulting in the growth or decay of the potential energy of a scale. This invokes sensible heat transfers from (or to) the other two scales or vice versa. Thus, intuitively, one possibility is that shorter scales describing the deep cumulus convective scales can transfer kinetic energy up the scale to the larger scale wind asymmetries of a hurricane. The potential energy generated by heating on cloud scales could perhaps be transferred up the scale to the potential energy of the larger scales. That potential energy of the larger scales can get converted to kinetic energy of the larger azimuthal scales by in-scale vertical overturning. The alternate possibility is that an organization of convection along the azimuthal coordinate can directly contribute to the growth of azimuthally averaged kinetic energy from the azimuthally averaged potential energy of the hurricane, and these upscale nonlinear transfers may not prove to be important for the driving of the hurricane scale. A purpose of this paper is to formally compute these interactions

among the cloud scales and the hurricane scales towards addressing the hurricane intensity issue from such possibilities (see section 5).

viii) $\langle K_s \cdot K_l \rangle$ is the nonlinear exchange of kinetic energy among different scales. This is another possible exchange of energy among waves. The equation for the kinetic energy exchange among different waves is nonlinear, and also invokes triple products. Thus, two waves from among the long waves can in principle interact with smaller cloud scales to provide nonlinear energy exchanges. These are exchanges among various waves in the azimuthal direction. Here the same trigonometric selection rules apply for these energy exchanges. For the hurricane intensity problem, we might be interested in the growth of kinetic energy of a low wave number such as 1 or 2 at the expense of other pairs of azimuthal waves. Triads such as 1, 7 and 8; 1, 8 and 9; 2, 15 and 13; 2, 12 and 10 are possible examples that satisfy the selection rules. Thus a pair of scales within the dimensions of clouds can in principle transfer energy to the higher wave numbers that describe a hurricane. This is a direct way by which a cloud scale can drive a hurricane scale. The possibility exists for such energy exchanges to go up or downscale, a formal computation, presented in section 5, clarifies these issues in the context of the model output.

ix) $\langle K_0 \cdot K_l \rangle$ - this is an exchange of kinetic energy between the azimuthally averaged flows and the long azimuthal wave numbers. This is akin to the familiar barotropic energy exchange. It invokes the covariance among the azimuthally averaged tangential motion and the eddy convergence of flux of momentum. This can go either way depending on the stabilizing or the destabilizing nature of the shear flows within the hurricane.

x) $\langle K_0 \cdot K_s \rangle$ - this is the same kind of energy as described in (ix) above except that shorter scales replace the azimuthal long waves. The mathematical formulation is the same as for (ix) above.

xi) $\langle P_o \cdot P_l \rangle$ is the potential energy exchange among azimuthally average flows and azimuthal long waves. This is analogous to a wave zonal exchange of potential energy. The direction of this exchange depends on the radial temperature gradients for wave number 0 and the radial transport and convergence of flux of heat (C_pT) by the long waves. The signs of computations dictate whether this heat transfer is up or down the thermal gradient.

xii) $\langle P_o \cdot P_c \rangle$ is the potential energy exchange among azimuthally averaged flows and shorter waves. The mathematical treatment of this exchange is presented in Appendix 1 and the explanation is the same as (xi) above except that long waves are to be replaced by shorter waves.

All these components of energetics presented in this paper were formulated using quasi-static primitive equations (see Appendix I for mathematical details of the formulation).

5. Results of Computations

a) Angular Momentum budget following inflowing trajectories in the storm relative frame of reference

In Fig. 8, we illustrate a trajectory of an air parcel constructed using the motion field (u, v, $\dot{\sigma}$) in storm relative coordinates. Also shown (in the blue isopleths) are the isotachs for a final map time August 25th at 00 UTC. This trajectory terminates in the vicinity of the velocity maxima of the hurricane at 850hPa level. Based on our forecasts this parcel originates on august 22nd at 00UTC from the 336 hPa level. A three-day motion of the parcel is illustrated here. This parcel generally descends from the upper troposphere to the 850hPa level.

We shall next illustrate in Table 2 the angular momentum budget following a parcel's history. This table shows the parcel's positions (as a function of time), the parcel's pressure, the pressure torque experienced over 12 hourly parcel motion segments, the angular momentum (M) of the parcel, the change in angular momentum (ΔM) across 12 hourly parcel motion segments, the net frictional torque experienced by the parcel along these segments and finally the effects of cloud torque in its contribution to the changes of angular momentum of the parcel. The pressure torques are generally small and are of the order of 10^{-6} m^2s^{-3}. The averaged pressure torque over 12 hourly trajectory segments was both positive and negative. The negative values are related to a beta gyre type asymmetry that the parcel encountered to the right of the storm motion where it moved towards higher pressure, $\frac{\partial z}{\partial \theta} > 0$. The net change in angular momentum for the inflowing parcel is negative throughout, since the parcel was moving closer to r=0 nearly always. The frictional torques above the 850 hPa surface arises from horizontal and vertical sub-grid scale diffusion in the free atmosphere, while above 850 hPa level these effects were small. The cloud torque is another manifestation of explicit frictional torques resolved by the model. These again are averaged values over the 12 hourly motion segments. These are based on explicit averages over the trajectory segments for the vertical eddy convergence and divergence of flux of momentum. The values along the trajectory, over all 12 hourly segments, is positive implying that cloud torques contributed to a net divergence of eddy flux of momentum of the parcel. This acts to reduce the angular momentum for the inflowing parcel. It is also clear from the table that the largest change of the angular momentum (in storm relative coordinates) arises for parcel encountering such cloud turbulence.

Explicit friction is that part of the model friction that comes from the parameterization of the surface layer and the planetary boundary layer physics. Furthermore, we include the model's

vertical diffusion of momentum. These are all explicitly coded within the MM5 model's formulation. We contrast the resolved cloud friction and cloud frictional torques with the "cloud torques". The frictional torques ($F_\theta r$) were calculated at each level and interpolated onto the space-time segments along the trajectories. The frictional torque largely reflects its contribution to loss of outer angular momentum by the surface friction and its vertical disposition. This is larger as we approach the storm's center where the surface winds are stronger. The pressure torques in a non-hydrostatic model generally reflects the presence of clouds in the model. The pressure of liquid water (overload) and vertical acceleration contribute to vertical acceleration of the order of 10^{-4} to 10^{-5} ms^{-2} over such regions. Pressure perturbations of the order of a hPa are found in the model output over such regions. The pressure field is not entirely radially symmetric but shows some interesting departures, as shown in Fig. 9 where the 3-day forecast of seal level pressure distribution for Hurricane Bonnie from the model run is illustrated. Parcels passing through such regions encounter large pressure torques. Over the entrance and exit region of such deep convective elements the pressure torques tend to be opposite in sign, thus canceling out any net significant contribution. The explicit cloud torque turned out to be a major contributor to the diminution of the outer angular momentum of inflowing parcels. The essential angular momentum of the air at the destination point (at hour 72) is largely influenced by these cloud torques. The cloud torques are contributed by $-r\frac{\partial}{\partial z}\overline{u^1 w^1}$, where the vertical eddy flux convergence of momentum is explicitly resolved by the cloud scale motions. A net divergence of flux of momentum by the clouds contributes to negative values of $(\Delta M)_c$ and a net diminution of angular momentum along the segments as noted in the trajectory (Table 2). These explicitly resolved clouds by the mesoscale model reduce the outer angular momentum considerably (by as much as 40%), thus ending up providing an intensity of 45 ms^{-1} for the

storm's highest winds. These back trajectories were deliberately constructed from the regions of the strong winds to the storm exterior. We are only showing the history of one parcel here, several such trajectories were in fact constructed that essentially confirmed these same results.

Figures 10 a,b,c,d,e illustrate computations relevant to the 'cloud torques'. Here results between hours 48 to 49 of a forecast trajectory are considered. This segment of the one-hour trajectory contains roughly 301 sub-intervals over which relevant model output data is illustrated here. In Fig. 10a we present the vertical velocity along this cloud element. The vertical velocity reaches almost 10 ms^{-1} near sub-interval 100. This is one of the inner deep convective cloud elements of the hurricane. The corresponding values of $W'\theta'$ at two vertical levels (500 hPa and 600 hPa) for this cloud segment are shown in Figs. 10b and 10c respectively. Strong positive values of the vertical eddy flux of momentum are of the order of 30 m^2s^{-1} with an increase of the eddy flux at the upper level by roughly 3 units within the cloud. This leads to a net divergence of flux of momentum and a measurable cloud torque (negative value) in Fig. 10d. This contributes to a sizeable reduction of the absolute angular momentum along the inflowing trajectory from the cloud scale turbulence. The largest negative value within the cloud is of the order of –90 m^2s^{-3}. Cloud turbulence does also contribute to a smaller net increase, 50 units, downstream from the region of maximum ascent. This is just one example of the so called 'cloud torque' for a single cloud element. The many simulated deep convective cloud elements collectively play an important role in determining the inner angular momentum and thus on the storm's intensity. Figure10e shows a longer trace along a three hour trajectory (between hours 48 and 51) of $W'V_\theta'$ that illustrates the nature of the cloud turbulence in a hurricane model. The mean value of $W' V_\theta'$ during these 3 hours is around $+7\ m^2\ sec^{-2}$, that shows that clouds at this level (600 hPa) contribute to a net upward flux of momentum.

b) Scale Interactions

We have formulated the energetics for a quasi-static system. Since the storm was over the ocean, the use of a pressure coordinate was felt quite suitable. The quasi-static components of the data sets were easily derived from the model's earth following sigma to the pressure coordinate system. We shall first present the results for these processes that invoke quadratic in-scale energy conversions. All of the results presented here are in storm-centered cylindrical coordinates and are mass integrals between radii r_1 and r_2, around the azimuthal coordinate, and between 100 hPa and the earth surface.

i) Generation of Available Potential Energy

This is measured by the covariances of heating and temperature and is expressed by

$$<\mathrm{H,T}> = \int_m \gamma HT dm\ ,\ \gamma = -\frac{\theta}{T}\left(\frac{R}{C_p p}\right) / \frac{\partial \bar{\theta}}{\partial p} \qquad (7)$$

where γ is a static stability parameter, and $\bar{\theta}$ is a surface area averaged potential temperature. γ varies with pressure. The covariance HT can be broken down into in-scale harmonic components,

$$HT = H_o T_o + H_1 T_1 + ... H_n T_n \qquad (8)$$

where o denotes the azimuthally averaged contribution and 1 denotes the first harmonic. Hence, the net generation can be expressed by $\int_m \gamma \sum_{i-0}^{n} H_i T_i dm$. The results of these computations are shown in Figs. 11a,b,c,d,e,f. The different panels show the results from forecasts for hours 6 through 72. Within each panel, the results of computations averaged over cylindrical mass elements from r=0 to r=40 km, r=40 km to r=200 km, and r=200 to r=380 km are displayed. These carry the mass integrals of the generation term within these domains. Separate histograms

are presented for the azimuthally averaged wave number 0, wave numbers 1 and 2, wave numbers 0, 1, and 2 and wave numbers 3 through 180. These results show that the largest generation occurs at wave number 0. Wave numbers 1 and 2 contribute about one third of the total generation of the eddy available potential energy. The contributions from the other scales are much smaller. The warm core of the model hurricane extends from roughly r=0 to r=180 km. The heating within this region and the cooling outside of this region contributes to the hurricane scale generations of APE for wave numbers 0, 1, and 2. Clearly, the cloud scale heating transcends to the hurricane scales from the organization of convection. This breakdown among scales is essentially similar during the entire 72 hours of the model run. There appears to be a direct generation of available potential energy on the hurricane scale, this evidently is a result of the organization of convection on the hurricane scales.

ii) Generation of Kinetic Energy from Vertical Overturning

The total contribution of eddy kinetic energy over a mass m is given by:

$$<\text{PE,KE}> = -C_p \int_m \frac{W'T'}{p} dm \qquad (9)$$

This is a quadratic non-linearity, hence we can express it as $-C_p \int_m \frac{1}{p} \sum_n W_n T_n dm$ where n denotes azimuthal wave numbers. Thus, it is possible to separately evaluate the contributions for each wave number. We can also separately evaluate the contributions for the azimuthally averaged component (i.e. wave number zero), i.e. $-C_p \int_m \frac{W_o T_o}{p} dm$. These are contributions from "in-scale" vertical overturnings that generate kinetic energy. Since each active deep convective element with scales of the order of a few km has its strongest upward and downward motions on the cloud scale, we might expect to see a large contribution for these smaller scales. However, the

organization of convection is more robust than the size of a single cloud, these contributions seem to prefer the hurricane scale (i.e. azimuthal wave numbers 0, 1, and 2), reflecting the organization of convection. This is shown in Figs. 12a,b,c,d,e,f. The histograms reflect the results over the same three regions as in Fig. 11. The different panels (a, b, c, d, e, and f) show the results from the forecast data sets for hours 6 through 72 at intervals of 6 hours. The histograms in each panel show the energy conversions (potential to kinetic) for wave number 0, wave numbers 1 and 2, wave numbers 0, 1, and 2 and the rest of the waves. The results are quite similar at all these forecast intervals. The largest contribution is found at the azimuthally averaged wave number 0. This shows that clouds have an organization along the circular geometry, thus shifting the scale of overturning from the cloud scales (few km) to the hurricane scale. The conversion for wave numbers 1 and 2 are about half as large as those for wave number 0. If we identify wave numbers 0, 1, and 2 as the hurricane scales, we see a substantial conversion of APE into EKE on this scale, again attributed to this large-scale organization of convection. The contribution for wave numbers 3 through 180 was in fact quite small and even fluctuating in sign for different smaller scales. The energetics in the wave number domain for the middle latitude zonally averaged jet, wave number 0, is opposite to that for a hurricanes azimuthal wave number 0. Waves provide energy to the wave number 0 in the former case whereas they seem to remove the energy from the hurricane circulation. The former is generally regarded as a low Rossby number phenomenon whereas the latter is clearly one where the Rossby number exceeds one.

iii) Energy exchanges due to non-linear triad interactions

In Figs. 13a,b we show the gain or loss of energy for wave numbers 1 and 2 for the eddy kinetic energy (Fig. 13a) and eddy potential energy (Fig. 13b) in units m^2s^{-3}, that arise from

interactions of these scales with all other permitted scales. Along the abscissa we show the forecast hours. The results shown here are vertically integrated values through the troposphere over the three different regions, i.e., inner, middle and outer radii bound. The obvious result is a net loss of energy at all radii for the hurricane scale (wave numbers 1 and 2) from these scale interactions. The largest losses occur at hour 72 when the storm had the strongest intensity. The cascade is strongest for wave number 1 when it interacts with other permitted scales.

iv) Summary of overall energy exchanges in the azimuthal wave number domain

The overall results of the energy exchanges are summarized in Fig. 14. These are 72 hour averages during this entire time Bonnie had hurricane wind strength. These are mass averaged energy exchanges based on the equations given in Appendix 1. The vertical integrals cover the atmosphere between the ocean surface and the 100 hPa level. Three colors distinguish the results over different radial belts: Red denotes an inner area 0 to 40 km. Green denotes a fast wind region 40-200 km. Blue denotes an outer area 200-380 km. All units of energy exchange are normalized to m^2/s^3. Three categories of energy exchange are grouped here: (a) Azimuthally averaged wave number 0, (b) Azimuthal long waves, wave numbers 1 and 2 and (c) Azimuthal short waves, wave numbers 3 to 180. The first two categories are designated as the hurricane scales, the third one is arbitrarily labeled as the cloud scales although this naming is not entirely correct.

For all of these scales the generation of available potential energy from heating and the conversion of available potential energy to eddy kinetic energy is described by the in-scale processes. These are interestingly the largest in the inner 40 km radii for wave number 0. That reflects the hurricane scale organization of heating and of the covariances of heating and temperature, and vertical velocity and temperature. This arises from the organization of clouds

along azimuthal wave number 0. The next in magnitude are contribution for the long waves where again clearly there is a contribution form the organization of clouds on the azimuthal wave numbers 1 and 2. The combined contribution for wave numbers 3 to 180 is less than 10 percent of those for wave number 0. The largest values of the generation of PE and its conversion to KE occur at the inner radii $0 < r < 40$ km. This is the region of the heaviest rains in the MM5 model's simulation of Hurricane Bonnie. The values fall off rapidly as we proceed to the outer radial belts.

The barotropic energy exchange comprises kinetic energy exchange from wave number 0 to the other waves. The long waves essentially extract energy from the azimuthally averaged wave number 0, whereas the so-called cloud scales in fact supply energy to wave number 0. Among these, some of the largest barotropic energy exchanges are from the wave number 0 to the long waves. At the different radial belts these values range from 78.6 to 58.4 to 30.75 units. This shows that the hurricane scale (azimuthally averaged wave number 0) is bartropically unstable to the long wave scales (wave numbers 1 and 2). Thus we can infer that the large-scale asymmetries in the hurricane's intense motion can arise from barotropic dynamics - that is in addition to the possible translation asymmetry, which arise from the motion of a symmetric vortex in a uniform steering flow. This kinetic energy exchange from the wave number 0 to the long wave is largest in the inner radial belt 0 to 40 km where the maxima of the cyclonic vorticity of the hurricane reside. The kinetic energy exchange from the cloud scales to the wave number 0 is largest at the outer radii r >200 km. As we move to these outer radii, the cloud scales exhibit an increasing convergence of flux of momentum $\overline{V_{rn}V_{\theta n}}$ that seems to increase its contribution for the barotropic stabilization.

The other areas of energy exchange are the kinetic to kinetic and potential-to-potential. These are the nonlinear three-component exchanges among different scales. The arrows connecting K_l *to* K_c and P_l *to* P_c show the collective exchanges from the long to the sort wave scales summarized here. This is essentially a cascading process where energy is conveyed from the larger to the smaller scales. The kinetic energy exchange K_l *to* K_c is much larger in magnitude compared to those of P_l *to* P_c. The inner radial belt 0 <r <40 km carries the largest non linear energy transfers. There are also potential energy exchanges between the azimuthally averaged wavenumber 0 and the waves. Those exchanges are all directed from waves to the wave number 0. The largest such exchanges are at the inner radii $0 \leq r \leq 40$ km. The magnitude of the energy transferred by the long waves are larger compared to that from the short waves to the zonal. These exchanges are related to the radial transfer of heat (up the gradient) towards wave number zero. The longer waves seem more efficient in reinforcing the warm core of the hurricane in this sense. This is the overall energy exchange scenario from the very high-resolution simulation of hurricane Bonnie of 1998.

6. Concluding Remarks

The hurricane intensity issue is among the major unsolved scientific problems presently. This paper merely presents two possible frameworks - scale interactions among clouds and hurricane, and an angular momentum perspective for this problem. The deep convective elements within a hurricane have dimension of the order of a few km each. The role of cloud scale heating, generation of available potential energy and its transformation to eddy kinetic energy can only be an in-scale (i.e. individual cloud scale) process since these processes involve quadratic non-linearities. The quadratic non-linearities are the covariances among heating and temperature, and vertical velocity and temperature. If that were so, then the only avenue for that

energy to drive the hurricane would be through non-linear triad interactions between kinetic and kinetic energy, and available potential to available potential energy among cloud scales and the hurricane scale. That naïve picture is not what is borne out by the computations based on data sets derived from meso-scale non-hydrostatic microphysical models. The key finding is the organization of convection on the azimuthally averaged wave number 0 and the large scale asymmetric scales of the hurricane, i.e. wave numbers 1 and 2 precedes all that. Those scales are inferred from the decomposition of the liquid water mixing ratio fields that carry clearly the deep convective cloud signatures. The generation of potential energy and its transformation to kinetic energy thus takes place directly on the larger scales of the hurricane. This is brought about by the organization of convection - a topic that is not addressed in this paper. The other major component in the framework of scale interactions is the energy exchanges among scales via triad interactions. These are the exchanges from kinetic to kinetic and available to available potential energies. Those results among triplet of waves (hurricane scales and other scales) show largely a cascade of energy, i.e., hurricane scales lose energy when they interact with other scales. The issue of organization of convection can be addressed by starting from an unorganized pre-hurricane state and by a continual monitoring of the spectral form of the liquid water mixing ratio and its interactions with the rest of dynamics, physics and microphysics. Such a study can provide insights on the scale interactions that lead to an organization of convection. This study required a high resolution (up to 1 km) multiply-nested regional meso-scale model that resolves clouds explicitly. A recent version of the NCAR MM5 model (non-hydrostatic with microphysics) was used in this study.

A second aspect of this study was on the angular momentum perspective, on the torques that diminish the angular momentum along inflowing trajectories of air parcels. They reveal that

"cloud torques" play a major role in this diminution of outer angular momentum and in the eventual intensity of the hurricane that it attains. Since all of these findings are based on model output data sets, future studies on model sensitivity are needed on areas that impact the intensity the most. These are the vertical overturnings by organized convection and the cloud torques. This suggests that even details of microphysical parameterizations within clouds might require careful testing within these explicitly cloud resolving meso-scale models. Field experiments that carry out detailed measurements of microphysical parameters that affect the life cycle of clouds may also provide insights for model sensitivity studies.

Understanding of hurricane intensity may require a rather large model sensitivity studies on resolution (horizontal and vertical), data coverage, data assimilation, non convective rain (definition of threshold relative humidity), PBL physics, radiative transfer and clouds, and parameterizations within the equations of water vapor, cloud water, rain water, cloud ice, snow, groupel, and number concentrations of cloud ice.

7. Acknowledgements

The research work reported here was supported by NSF Grant No. ATM-0108741, NASA TRMM Grant No. NAG5-9662, NASA CAMEX Grant No. NAG8-1848, and FSU Research Foundation Grant No. 1338-895-45. We acknowledge the data support from the European Centre for Medium Range Weather Forecasts especially through the help of Dr. Tony Hollingsworth.

Appendix 1

The equations of motion in the storm-centered cylindrical coordinate system are

$$\frac{\partial v_\theta}{\partial t} = -v_\theta \frac{\partial v_\theta}{r\partial\theta} - v_r \frac{\partial v_\theta}{\partial r} - \omega \frac{\partial v_\theta}{\partial p} - \frac{v_r v_\theta}{r} - f v_r - g \frac{\partial z}{r\partial\theta} - F_\theta , \tag{1}$$

$$\frac{\partial v_r}{\partial t} = -v_\theta \frac{\partial v_r}{r\partial\theta} - v_r \frac{\partial v_r}{\partial r} - \omega \frac{\partial v_r}{\partial p} - \frac{{v_\theta}^2}{r} + f v_\theta - g \frac{\partial z}{\partial r} - F_r , \tag{2}$$

and the continuity equation is

$$0 = -\frac{\partial v_\theta}{r\partial\theta} - \frac{\partial v_r}{\partial r} - \frac{v_r}{r} - \frac{\partial \omega}{\partial p} . \tag{3}$$

The independent variables in this coordinate system are the azimuthal angle θ, the radial distance from the center r, and the pressure p. The tangential and radial winds are v_θ (positive anticlockwise) and v_r (positive outward), respectively. The vertical velocity in pressure coordinates is ω, f is the Coriolis parameter, gz is the geopotential height, and F_θ and F_r are the tangential and radial components of the frictional force per unit mass. Any of the dependent variables can be subjected to Fourier transform along the azimuthal (θ) direction:

$$f(\theta) = \sum_{n=-\infty}^{\infty} F(n) e^{in\theta} , \tag{4}$$

where the complex Fourier coefficients $F(n)$ are given by

$$F(n) = \frac{1}{2\pi} \int_0^{2\pi} f(\theta) e^{-in\theta} d\theta . \tag{5}$$

The Fourier transform of the product of two functions is given by

$$\frac{1}{2\pi} \int_0^{2\pi} f(\theta) g(\theta) e^{-in\theta} d\theta = \sum_{m=-\infty}^{\infty} F(n) G(n-m) . \tag{6}$$

Let us consider only the non-linear terms in Eqs. (1) and (2). If we multiply both equations by $\frac{1}{2\pi} e^{-in\theta}$, integrate along an azimuthal circle, and apply (4), (5) and (6), we obtain

$$\frac{\partial V_\theta(n)}{\partial t} = -\sum_{m=-\infty}^{\infty} \frac{imV_\theta(m)}{r} V_\theta(n-m) + \left(\frac{\partial V_\theta(m)}{\partial r} + \frac{V_\theta(m)}{r} \right) V_r(n-m) + \frac{\partial V_\theta(m)}{\partial p} \Omega(n-m), \tag{7}$$

$$\frac{\partial V_r(n)}{\partial t} = -\sum_{m=-\infty}^{\infty} \left(\frac{imV_r(m)}{r} - \frac{V_\theta(m)}{r} \right) V_\theta(n-m) + \frac{\partial V_r(m)}{\partial r} V_r(n-m) + \frac{\partial V_r(m)}{\partial p} \Omega(n-m), \tag{8}$$

where $V_\theta(n)$, $V_r(n)$, and $\Omega(n)$ are the nth Fourier coefficients of v_θ, v_r, and ω. From the continuity equation we get

$$\frac{\partial \Omega(n)}{\partial p} + \frac{inV_\theta(n)}{r} + \frac{\partial V_r(n)}{\partial r} + \frac{V_r(n)}{r} = 0. \tag{9}$$

By multiplying (7) and (8) with $V_\theta(-n)$ and $V_r(-n)$, and the complex conjugates of (7) and (8) with $V_\theta(n)$ and $V_r(n)$, respectively, we obtain

$$\begin{aligned} \frac{\partial |V_\theta(n)|^2}{\partial t} = &-\sum_{m=-\infty}^{\infty} \frac{imV_\theta(m)}{r} \left(V_\theta(-n)V_\theta(n-m) + V_\theta(n)V_\theta(-n-m) \right) \\ &+ \left(\frac{\partial V_\theta(m)}{\partial r} + \frac{V_\theta(m)}{r} \right) \left(V_\theta(-n)V_r(n-m) + V_\theta(n)V_r(-n-m) \right) \\ &+ \frac{\partial V_\theta(m)}{\partial p} \left(V_\theta(-n)\Omega(n-m) + V_\theta(n)\Omega(-n-m) \right) \end{aligned} \tag{10}$$

$$\begin{aligned} \frac{\partial |V_r(n)|^2}{\partial t} = &-\sum_{m=-\infty}^{\infty} \left(\frac{imV_r(m)}{r} - \frac{V_\theta(m)}{r} \right) \left(V_r(-n)V_\theta(n-m) + V_r(n)V_\theta(-n-m) \right) \\ &+ \frac{\partial V_r(m)}{\partial r} \left(V_r(-n)V_r(n-m) + V_r(n)V_r(-n-m) \right) \\ &+ \frac{\partial V_r(m)}{\partial p} \left(V_r(-n)\Omega(n-m) + V_r(n)\Omega(-n-m) \right) \end{aligned} \tag{11}$$

Now if we apply (9) and add (10) and (11), we obtain an expression for the local rate of change of kinetic energy of wave number n due to non-linear interactions as:

$$\frac{\partial K(n)}{\partial t} = \sum_{\substack{m=-\infty \\ m\neq 0}}^{\infty} V_\theta(m)\left(\frac{1}{r}\Psi_{v_\theta \frac{\partial v_\theta}{\partial \theta}}(m,n) + \Psi_{v_r \frac{\partial v_\theta}{\partial r}}(m,n) + \Psi_{\omega \frac{\partial v_\theta}{\partial p}}(m,n) + \frac{1}{r}\Psi_{v_\theta v_r}(m,n)\right)$$
$$+ V_r(m)\left(\frac{1}{r}\Psi_{v_\theta \frac{\partial v_r}{\partial \theta}}(m,n) + \Psi_{v_r \frac{\partial v_r}{\partial r}}(m,n) + \Psi_{\omega \frac{\partial v_r}{\partial p}}(m,n) - \frac{1}{r}\Psi_{v_\theta v_\theta}(m,n)\right) \qquad (12)$$
$$-\frac{1}{r}\frac{\partial}{\partial r} r\left[V_\theta(m)\Psi_{v_r v_\theta}(m,n) + V_r(m)\Psi_{v_r v_r}(m,n)\right] - \frac{\partial}{\partial p}\left[V_\theta(m)\Psi_{\omega v_\theta}(m,n) + V_r(m)\Psi_{\omega v_r}(m,n)\right]$$

where $\Psi_{ab}(m,n) = A(n-m)B(-n) + A(-n-m)B(n)$.

The last term in (12) vanishes upon integration from top to bottom of the atmosphere, provided $\omega(p_{top}) = \omega(p_{bottom}) = 0$. With a similar approach, we can find the rate of change of potential energy due to non-linear interactions in a cylindrical coordinate system. The local change in temperature is given by

$$\frac{\partial T}{\partial t} = -v_\theta \frac{\partial T}{r\partial \theta} - v_r \frac{\partial T}{\partial r} - \omega \frac{\partial T}{\partial p} + \frac{RT}{C_p p}\omega + \frac{Q}{C_p} \qquad (13)$$

If we denote the Fourier transform of T as B(n), multiply both equations by $\frac{1}{2\pi}e^{-in\theta}$, integrate along an azimuthal circle, and apply (4), (5) and (6), and consider only the non-linear terms, we obtain

$$\frac{\partial B(n)}{\partial t} = -\sum_{m=-\infty}^{\infty} \frac{imB(m)}{r} V_\theta(n-m) + \frac{\partial B(m)}{\partial r} V_r(n-m) + \left(\frac{\partial B(m)}{\partial p} - \frac{RB(m)}{C_p p}\right)\Omega(n-m). \qquad (14)$$

Following the same procedure as for (13), and defining the available potential energy as $P(n) = C_p \eta |B(n)|^2$, where $\eta = -\frac{R^2}{C_p p^{R/C_p}}\left(\frac{\partial \Theta}{\partial p}\right)^{-1}$ is the static stability factor, we obtain

$$\frac{\partial P(n)}{\partial t} = C_p \eta \sum_{\substack{m=-\infty \\ m\neq 0}}^{\infty} B(m)\left(\frac{1}{r}\Psi_{v_\theta \frac{\partial T}{\partial \theta}}(m,n) + \Psi_{v_r \frac{\partial T}{\partial r}}(m,n) + \Psi_{\omega \frac{\partial T}{\partial p}}(m,n) + \frac{R}{C_p p}\Psi_{\omega T}(m,n)\right) \qquad (15)$$
$$-\frac{1}{r}\frac{\partial}{\partial r} rB(m)\Psi_{v_r T}(n,m) - \frac{\partial}{\partial p} B(m)\Psi_{\omega T}$$

as the expression for the local rate of change of the available potential energy of frequency n due to non-linear interactions with frequencies m and $n\pm m$. Similarly to (12), the last term vanishes upon integration over the depth of the atmosphere.

For azimuthal wave number zero the generation of available potential energy is given by:

$$G(P_0) = \int_m \gamma \left[H - \overline{\overline{H}}\right]\left[T - \overline{\overline{T}}\right] dm \tag{16}$$

where γ is a static stability parameter defined by

$$\gamma = -\frac{\theta}{T}\left(\frac{R}{C_p P}\right)\left(\frac{\partial \theta}{\partial P}\right)^{-1} \tag{17}$$

The double over bars indicate a horizontal area average and the square bracket is an azimuthal mean. H is the heating rate and T is the temperature. The generation at any wave number is simply expressed by

$$G(n) = \int_m \gamma\, H_n\, T_n\, dm \tag{18}$$

This is what is used for each wave within the long and the shorter scale waves. For azimuthal wave number zero the conversion of potential to kinetic energy is given by:

$$\langle P_0 \cdot K_0 \rangle = -\int_m C_P \frac{\left[\omega_0 - \overline{\overline{\omega}}\right]\left[\mathrm{T}_0 - \overline{\overline{T}}\right]}{P} dm \tag{19}$$

and for all other scales:

$$\langle P_n \cdot K_n \rangle = -\int_m C_P \frac{\omega_n T_n}{P} dm \tag{20}$$

Here ω is the vertical velocity. The exchange among azimuthally averaged flows and other waves are expressed by the following equations:

$$< K(0)\cdot K(n) >= \int_M \left\{ \sum_{n=1}^{\infty} \left(\Phi_{uv}(n) \frac{\cos\varphi}{a} \frac{\partial}{\partial\varphi} \left(\frac{\overline{u}}{\cos\varphi} \right) + \Phi_{vv}(n) \frac{1}{a} \frac{\partial \overline{v}}{\partial\varphi} + \Phi_{u\omega}(n) \frac{\partial \overline{u}}{\partial p} + \Phi_{v\omega}(n) \frac{\partial \overline{v}}{\partial p} - \Phi_{uu}(n) \overline{v} \frac{\tan\varphi}{a} \right) \right.$$
$$\left. - \frac{g}{a} \overline{v} \frac{\partial z}{\partial\varphi} - \overline{d} \right\} dM$$

and (21)

$$< P(0)\cdot P(n) >= \int_M \left\{ \sum_{n=1}^{\infty} \left(C_p \eta \Phi_{Tv}(n) \frac{\partial \overline{T}}{\partial\varphi} + \frac{\eta p^{\mu}}{\mu} \Phi_{T\omega}(n)'' \frac{\partial \overline{\theta}''}{\partial p} \right) + \frac{R}{p} \overline{\omega}\overline{T} + \eta\{\overline{T}''\overline{h}''\} \right\} dM \qquad (22)$$

where $\Phi_{ab}(n) = A(n)B(-n) + A(-n)B(n)$

These expressions (21) and (22) are used both for long and short wave exchanges with the azimuthally averaged flows.

References

Bao, J.-W., J. M. Wilczak, J.-K. Chio, and L. H. Kantha, 2000: Numerical simulation of air-sea interaction under high wind conditions using a coupled model: A study of hurricane development. Mon. Wea. Rev., **128**, 2190-2210.

Betts, A.K., and M.J. Miller, 1986: A new convective adjustment scheme. Part II: Single column test using GATE-wave, BOMEX, ATEX and Arctic airmass data sets. *Quart. J. Roy. Meteor. Soc.*, **112**, 693-709

Betts, A.K., and M.J. Miller, 1993: The Betts-Miller scheme. *The representation of cumulus convection in numerical models*, K.A. Emanuel and D.J. Raymond, Eds., Amer. Meteor. Soc., 246 pp.

Braun, S. A., 2002: A cloud-resolving simulation of Hurricane Bob (1991): Storm structure and eyewall buoyancy. *Mon. Wea. Rev.*, **130**, 1573-1592.

Braun, S. A., and W.-K. Tao, 2000: Sensitivity of high-resolution simulations of Hurriacne Bob (1991) to planetary boundary layer parameterizations. *Mon. Wea. Rev.*, **128**, 3941-3961.

Chen, Y.-S., and M. K. Yau, 2001: Spiral bands in a simulated hurricane. Part I: Vortex Rossby wave verification. *J. Atmos. Sci.*, **58**, 2128-2145.

Davis, C. A., and L. F. Bosart, 2001: Numerical simulations of the genesis of hurricane Diana (1984): Part I: Control simulation. *Mon. Wea. Rev.* **129**, 1859-1881.

Davis, C. A., and S. B. Trier, 2002: Cloud-resolving simulations of mesoscale vortex intensification and its effect on a serial mesoscale convective system. *Mon. Wea. Rev.* **130**, 2839-2858.

Deardorff, J. W., 1972: Parameterization of the planetary boundary layer for use in general circulation models, *Mon. Wea. Rev.*, **100**, 93-106.

Dudhia, J., 1989: Numerical study of convection observed during the winter monsoon experiments using a mesoscale two-dimensional model. *J. Atmos. Sci* , **46**, 3077-3107

Dudhia, J., 1993: A non-hydrostatic version of the Penn State–NCAR mesoscale model: Validation tests and simulation of an Atlantic cyclone and cold front. *Mon. Wea. Rev.*, **121**, 1493-1513.

Grell, G. A., J. Dudhia, and D. R. Stauffer, 1995: *A Description of the Fifth-Generation Penn State/NCAR Mesoscale Model (MM5).* National Center for Atmospheric Research, Boulder Colorado, 1995.

Hong, S.H., and H.L. Pan, 1996: Nonlocal boundary layer vertical diffusion in a medium-range forecast model. *Mon. Wea. Rev.*, **124**, 2322-2339.

Kamineni, R., T. N. Krishnamurti, R. A. Ferrare, S. Ismail, and E. V. Browell, 2003: Impact of high resolution water vapor cross-sectional data on hurricane forecasting. *Geophy. Res.Let.*, **30**, 1234.

Kamineni, R., T. N. Krishnamurti, S. Pattnaik, E. V. Browell, S. Ismail, R. A. Ferrare, 2004: Impact of CAMEX-4 Data sets For Hurricane Forecasts using a Global Model. (Submitted to JAS special issue on CAMEX4)

Krishnamurti, T.N. and Sheng Jian, 1985a: The heating field in an asymmetric hurricane – Part I: Scale Analysis. *Adv. Atmos. Sci.,* **2**, 402-413.

Krishnamurti, T.N. and Sheng Jian, 1985b: The heating field in an asymmetric hurricane – Part II: Results of computations. *Adv. Atmos. Sci.,* **2**, 426-445.

Krishnamurti, T.N., J. Xue, H.S. Bedi, K. Ingles and D. Oosterhof, 1991: Physical initialization for numerical weather prediction over the tropics. *Tellus*, **43**, 53-81.

Krishnamurti, T.N., C.M. Kishtawal, T. LaRow, D. Bachiochi, Z. Zhang, C.E. Williford, S. Gadgil and S. Surendran, 2000: Multi-model superensemble forecasts for weather and seasonal climate. *J. Climate*, **13**, 4196-4216.

Krishnamurti, T.N., S. Surendran, D.W. Shin, R. Correa-Torres, T.S.V. Vijaya Kumar, C.E. Williford, C. Kummerow, R.F. Adler, J. Simpson, R. Kakar, W. Olson and F.J. Turk, 2001: Real Time Multianalysis/Multimodel Superensemble Forecasts of Precipitation using TRMM and SSM/I Products. *Mon. Wea. Rev.,* **129**, 2861-2883.

Krishnamurti, T.N., D.R. Chakraborty, Nihat Cubukcu, L. Stefanova and T.S.V. Vijaya Kumar, 2003: A mechanism of the MJO based on interactions in the frequency domain. *Quart. J. Royal Met. Soc.*, **129**, 2559-2590.

Liu, Y., D.-L. Zhang and M.K. Yau, 1999: A multiscale numerical study of Hurricane Andrew (1992). Part II: Kinematics and inner-core structures. *Mon. Wea. Rev.*, **127**, 2597-2616.

Pasch, R.J., Avila, L.A., and Guiney, J.L., 2001: Atlantic Hurricane Season of 1998. Mon. Wea. Rev., **129**, 3085-3123.

Rizvi, S.R.H., Edward L. Bensman, T.S.V. Vijaya Kumar, Arun Chakraborty and T.N. Krishnamurti, 2002: Impact of CAMEX-3 data on the analysis and forecasts of Atlantic hurricanes. *Meteorol. Atmos. Phy.*, **79**, 13-32.

Saltzman, B., 1957: Equations governing the energetics of the larger scales of atmospheric turbulence in the domain of wave number. *J. Meteor.,* **14**, 513-523.

Saltzman, B., 1970: Large scale atmospheric energetics in the wave number domain. *Rev. Geophys. Space Phys.*, **8**, 289-302.

Williford, C.E., T.N. Krishnamurti, R. Correa-Torres, S. Cocke, Z. Christidis and T.S.V.V. Kumar, 2002: Real-Time Multimodel Superensemble Forecasts of Atlantic Tropical Systems of 1999. *Mon. Wea. Rev.*, **131**, 1878-1894.

Zhang, D.-L. and X. Wang, 2003: Dependence of Hurricane Intensity and Structures on Vertical Resolution and Time-Step Size. *Adv. Atmos. Sci.*, **20**, 711-725.

Figure Captions

Fig. 1: Observed and model predicted track of Hurricane Bonnie. Boxes in the illustration demonstrate the MM5 model nested grids at 27, 9, 3 and 1 km respectively.

Fig. 2. Visible Geostationary Operational Environmental Satellite-8(GOES-8) Satellite image of Hurricane Bonnie at 1615 UTC 23 Aug 1998.

Fig. 3. Initial distribution of (a) Sea Level Pressure (hPa), (b) Tangential Wind (ms^{-1}) and (c) Angular Momentum (m^2s^{-1}) of Hurricane Bonnie, valid on August 22, 1998 0000 UTC.

Fig. 4: Streamlines at 850 hPa derived from model output at (a) day-1, (b) day-2 and (c) day-3 of forecasts.

Fig. 5. Beta gyre structure for Hurricane Bonnie. Shown is the sea level pressure (hPa) distribution after removing the zonal (azimuthal) mean values.

Fig. 6. Distribution of rainwater mixing ratio (kg/kg) at 850 hPa for Hurricane Bonnie. (a) Day-2 Forecast, and (b) Day-3 Forecast.

Fig. 7. Power spectrum of variance of the liquid water mixing ratio at (a) initial time (t=1) and at (b) 24-hr forecast (t=2) for three different radii (0-40 km, the inner region; 40-200 km, the high wind region; and 200-380 km, the outer region) of Hurricane Bonnie.

Fig. 8. 72-hr 3-D backward trajectory of maximum wind at 850 hPa (ms^{-1}) for Hurricane Bonnie. Shown here is a trajectory terminating at the wind maxima in the vicinity of the center of the hurricane at the end of the 72-hr forecast. Isopleths in blue indicate the maximum wind distribution at 72-hr forecast time.

Fig. 9. 3-day sea level pressure (hPa) forecast of Hurricane Bonnie

Fig. 10. (a) Vertical velocity (ms^{-1}) at 500 hPa, (b) vertical eddy flux of momentum (units) at 500 hPa, (c) vertical eddy flux of momentum at 600 hPa and (d) cloud torque (units) during every time step of a one-hour forecast between 48^{th} and 49^{th} hour of model integration.

Fig. 11: Generation of available potential energy for Hurricane Bonnie. Three different histograms in each panel represent three regions – inner area (0-40 km), fast winds (40-200 km) and outer area (200-380 km). The panels from top to bottom are at different forecast times (a) 12 hr, (b) 24 hr, (c) 36 hr, (d) 48 hr, (e) 60 hr and (f) 72 hr of the model output.

Fig. 12: Generation of Kinetic Energy by vertical overturning for Hurricane Bonnie. Three different histograms in each panel represent three regions – inner area (0-40 km), fast winds (40-200 km) and outer area (200-380 km). The panels from top to bottom are at different forecast times (a) 12 hr, (b) 24 hr, (c) 36 hr, (d) 48 hr, (e) 60 hr and (f) 72 hr of the model output.

Fig. 13. Rate of change of (a) kinetic and (b) potential energy of wave numbers n=1 and n=2 due to interactions with pairs of waves with wave numbers (l,m) >2. Units are 10^{-5} m^2s^{-3}. The forecast hour is indicated along the abscissa.

Fig. 14. Summary of energy exchange computations resulting in the final intensity of Hurricane Bonnie. Different colors in the numbers represent three different regions of computations (Red for inner area between 0 and 40 km, Green for fast wind region between 40 and 200 km and Blue for outer area between 200 and 380 km of radius). Arrow marks indicate the direction of energy exchange.

List of Tables:

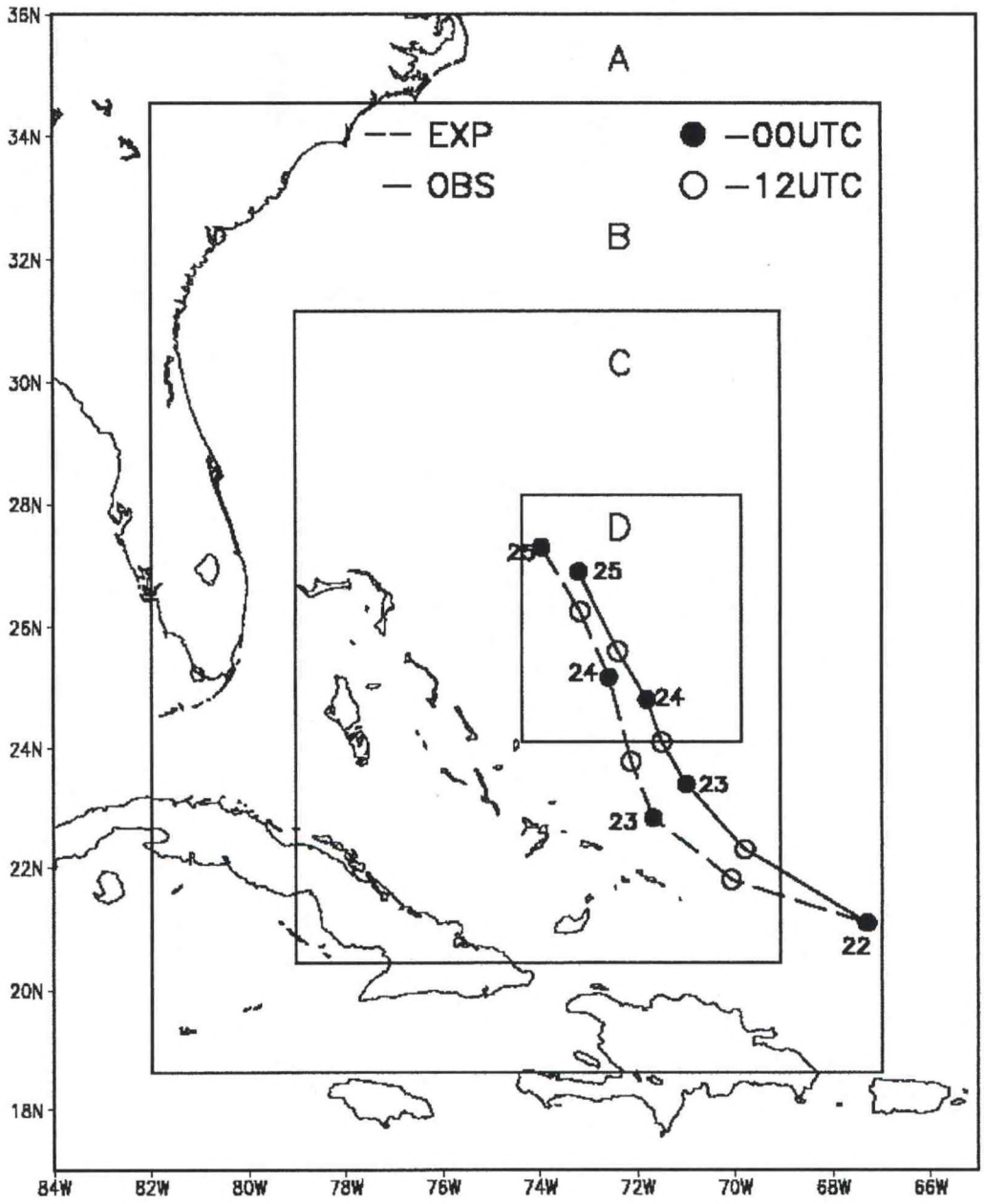

Fig. 1: Observed and model predicted track of Hurricane Bonnie. Boxes in the illustration demonstrate the MM5 model nested grids at (A) 27, (B) 9, (C) 3 and (D) 1 km respectively.

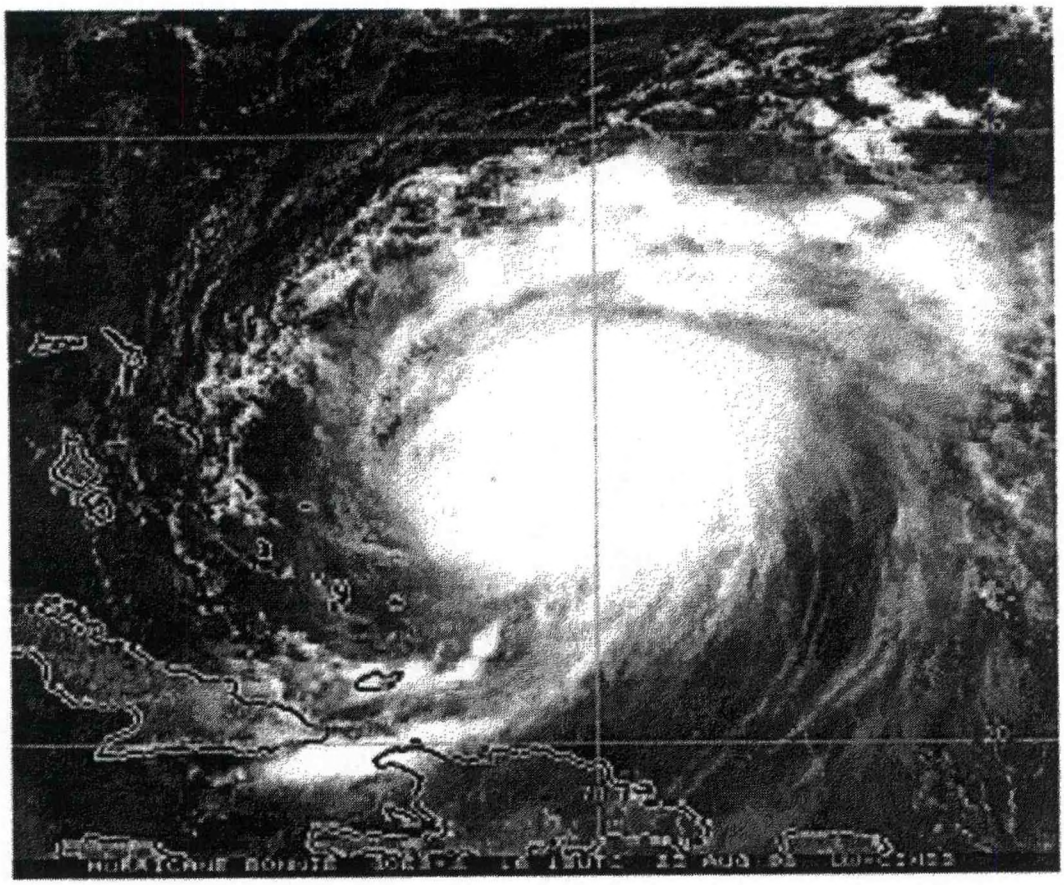

Fig. 2. Visible Geostationary Operational Environmental Satellite-8(GOES-8) Satellite image of Hurricane Bonnie at 1615 UTC 23 Aug 1998.

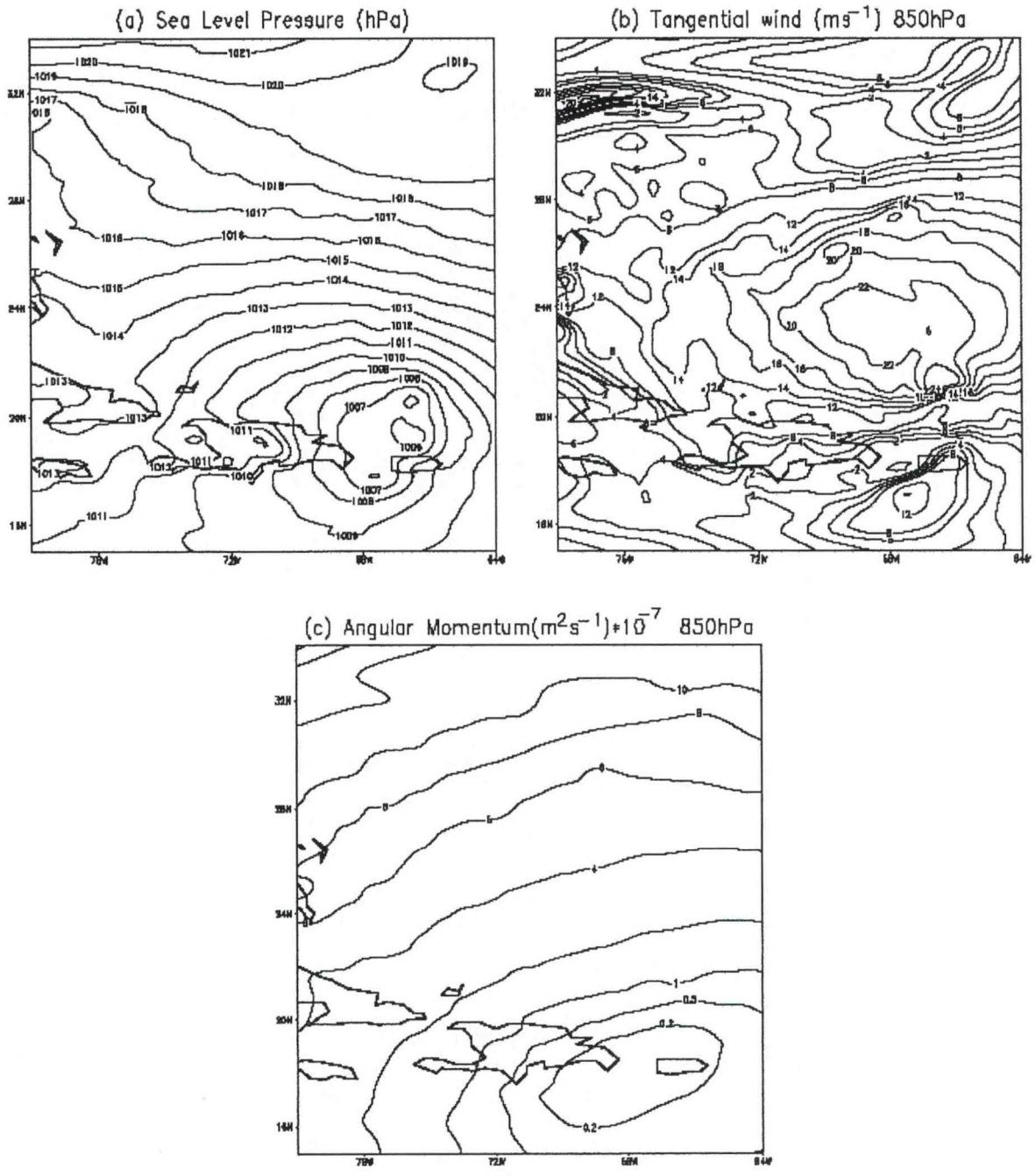

Fig. 3. Initial distribution of (a) Sea Level Pressure (hPa), (b) Tangential Wind (ms^{-1}) and (c) Angular Momentum (m^2s^{-1}) of Hurricane Bonnie, valid on August 22, 1998 0000 UTC.

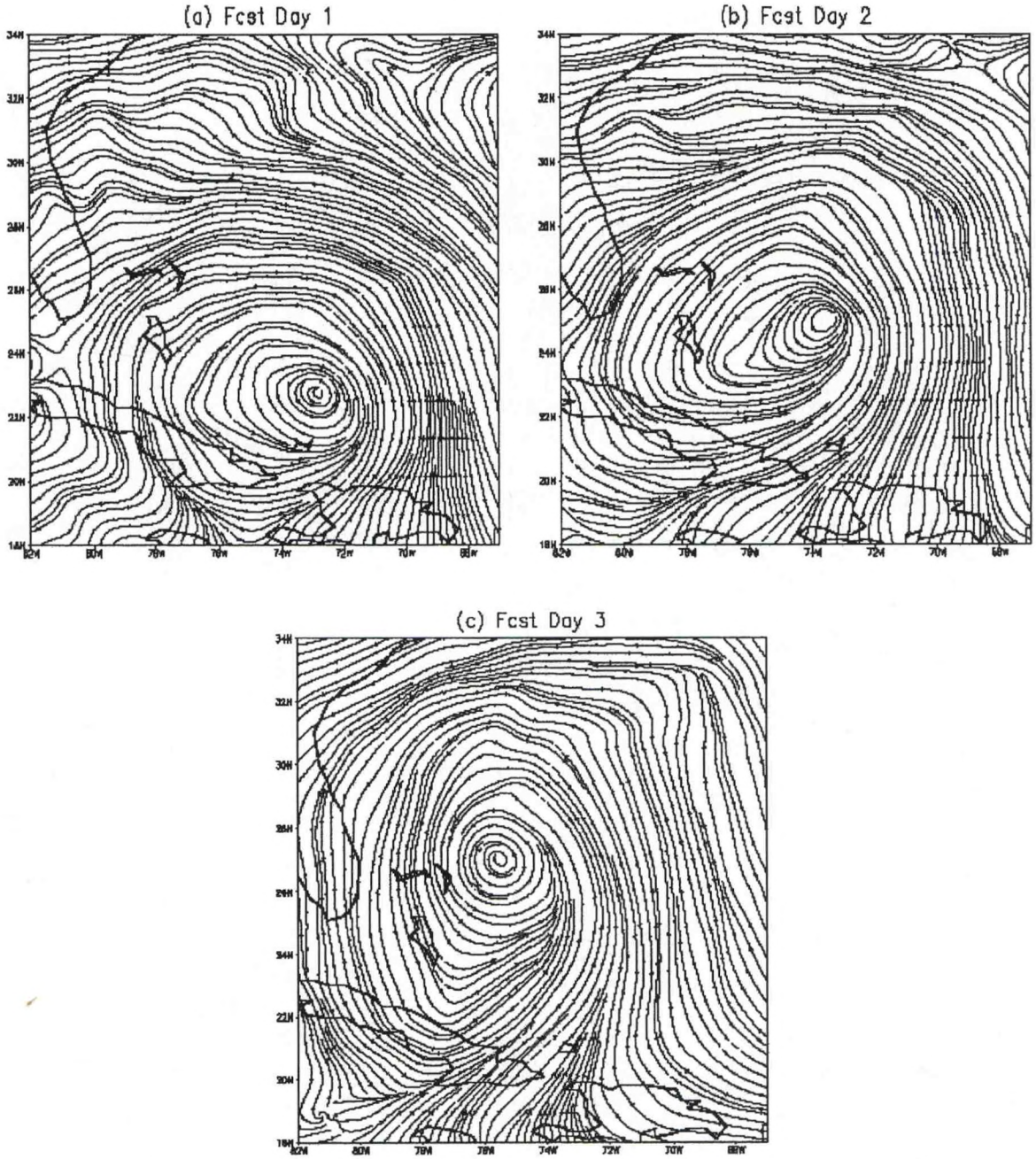

Fig. 4: Streamlines at 850 hPa derived from model output at (a) day-1, (b) day-2 and (c) day-3 of forecasts.

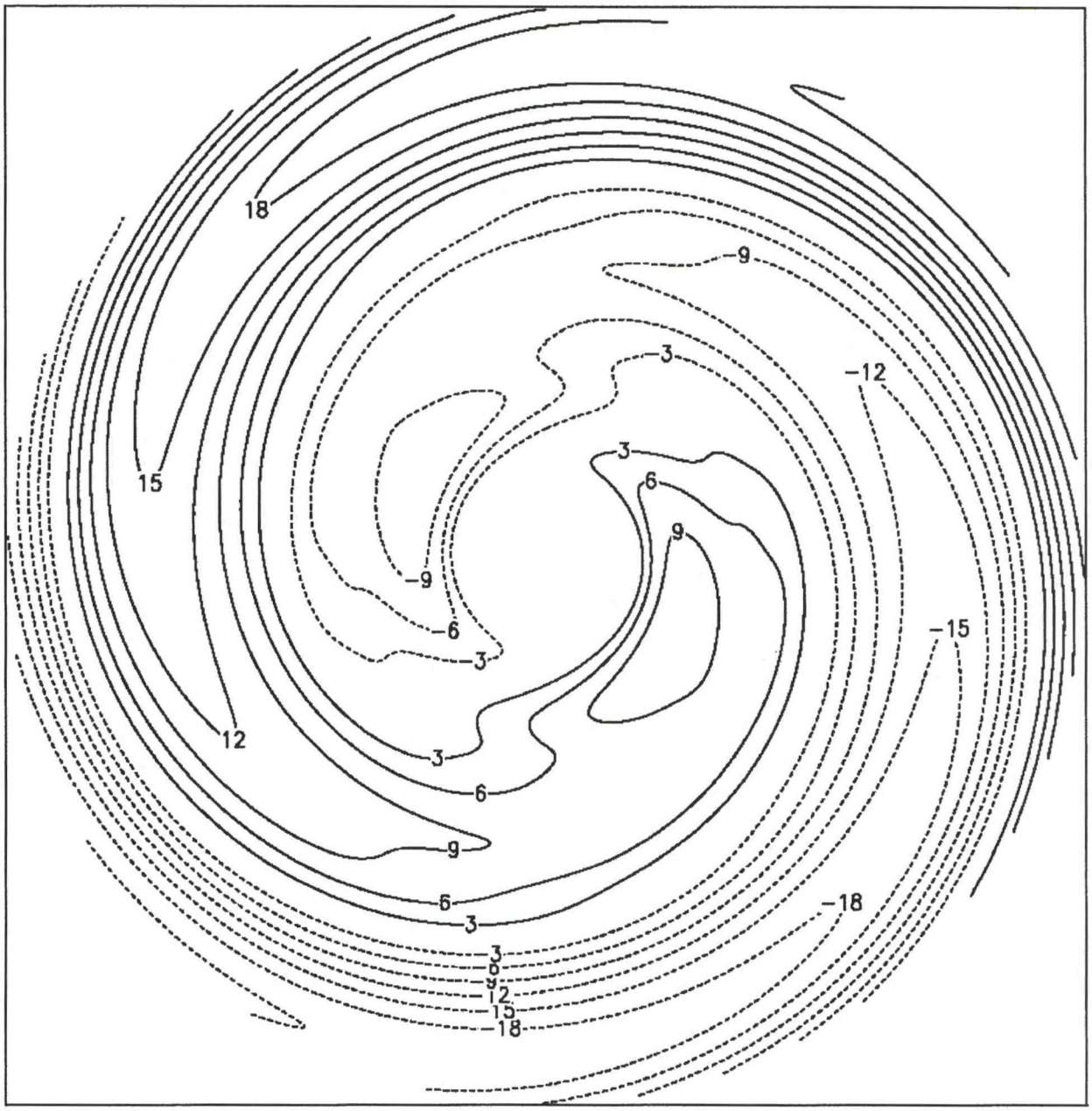

Fig. 5. Beta gyre structure for Hurricane Bonnie. Shown is the sea level pressure (hPa) distribution after removing the zonal (azimuthal) mean values.

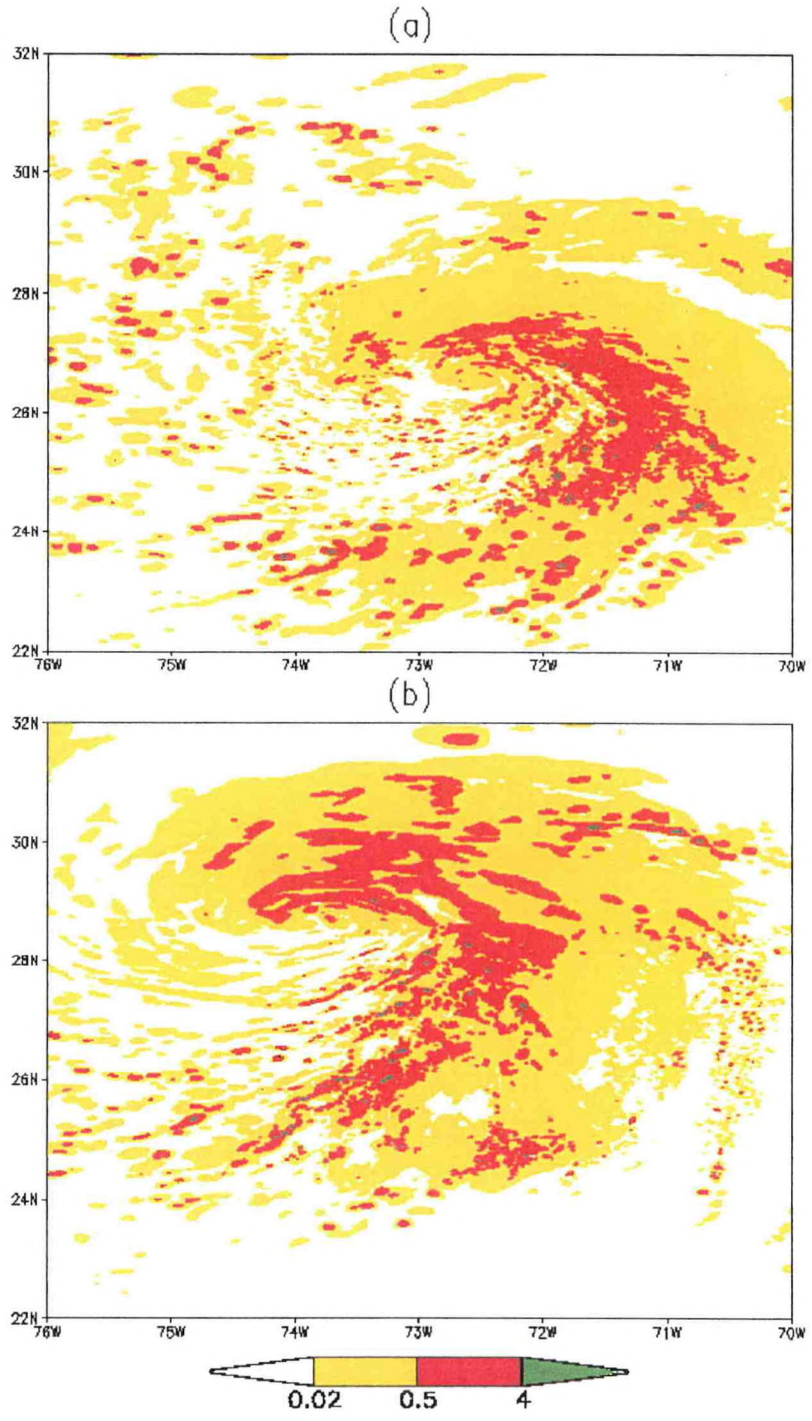

Fig. 6. Distribution of rainwater mixing ratio (kg/kg) at 850 hPa for (a) day-2 and (b) day-3 forecasts of Hurricane Bonnie.

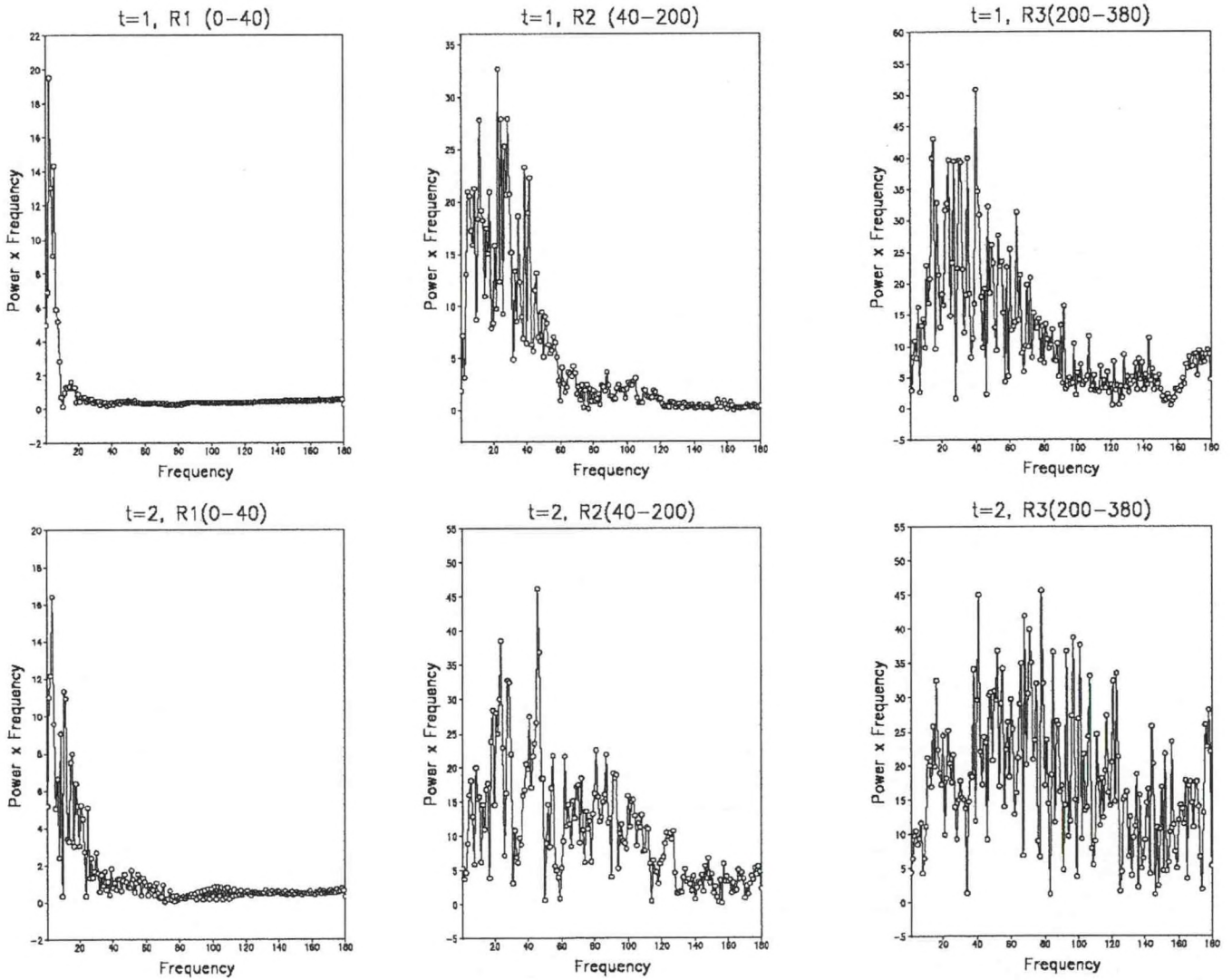

Fig. 7. Power spectrum of variance of the liquid water mixing ratio at initial time (t=1) and at 24-hr forecast (t=2) for three different radii (0-40 km, the inner region; 40-200 km, the high wind region; and 200-380 km, the outer region) of Hurricane Bonnie.

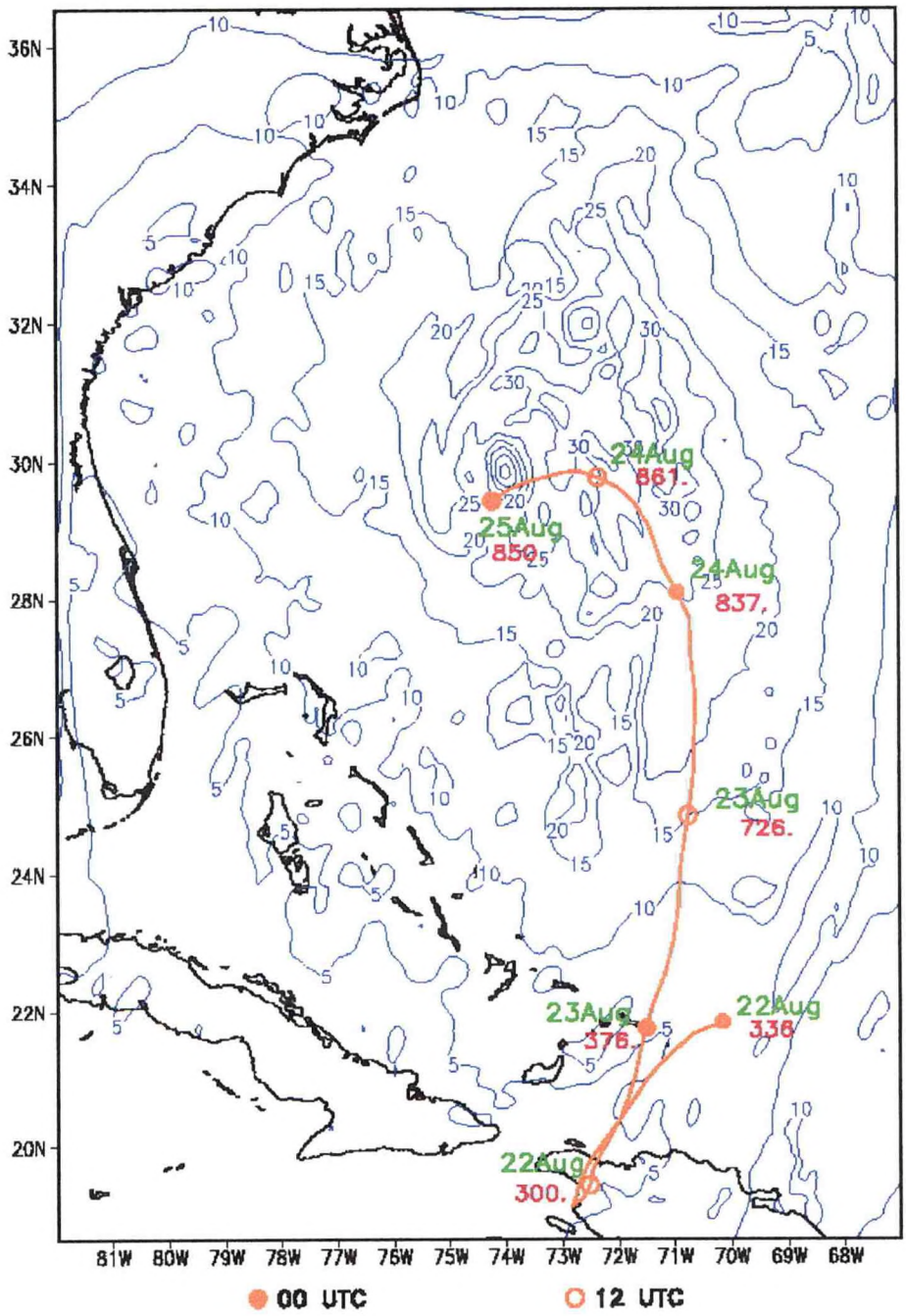

Fig. 8. 72-hr 3-D backward trajectory of maximum wind at 850 hPa (ms^{-1}) for Hurricane Bonnie. Shown here is a trajectory terminating at the wind maxima in the vicinity of the center of the hurricane at the end of the 72-hr forecast. Isopleths in blue indicate the maximum wind distribution at 72-hr forecast time.

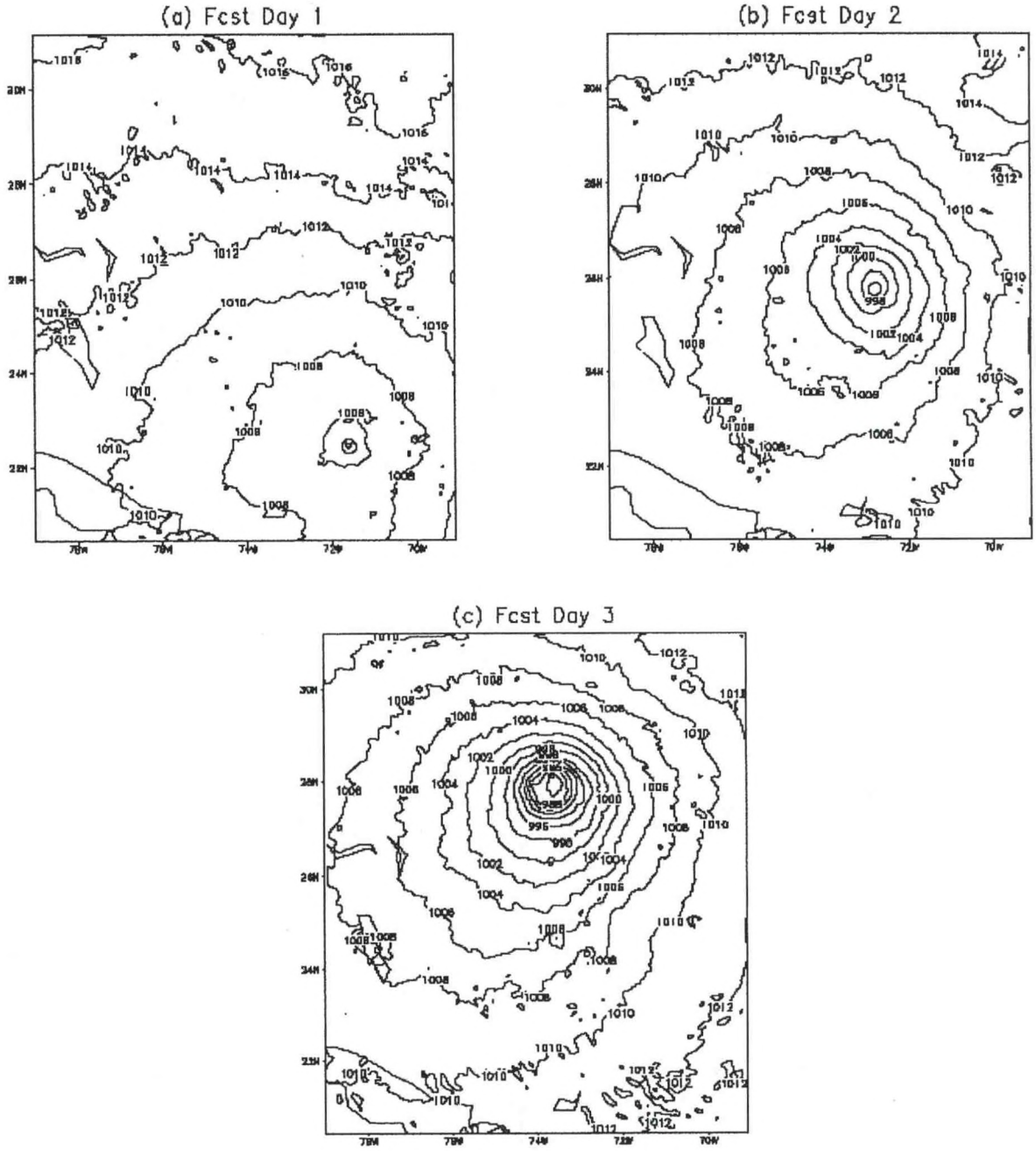

Fig. 9. 3-day sea level pressure (hPa) forecast of Hurricane Bonnie

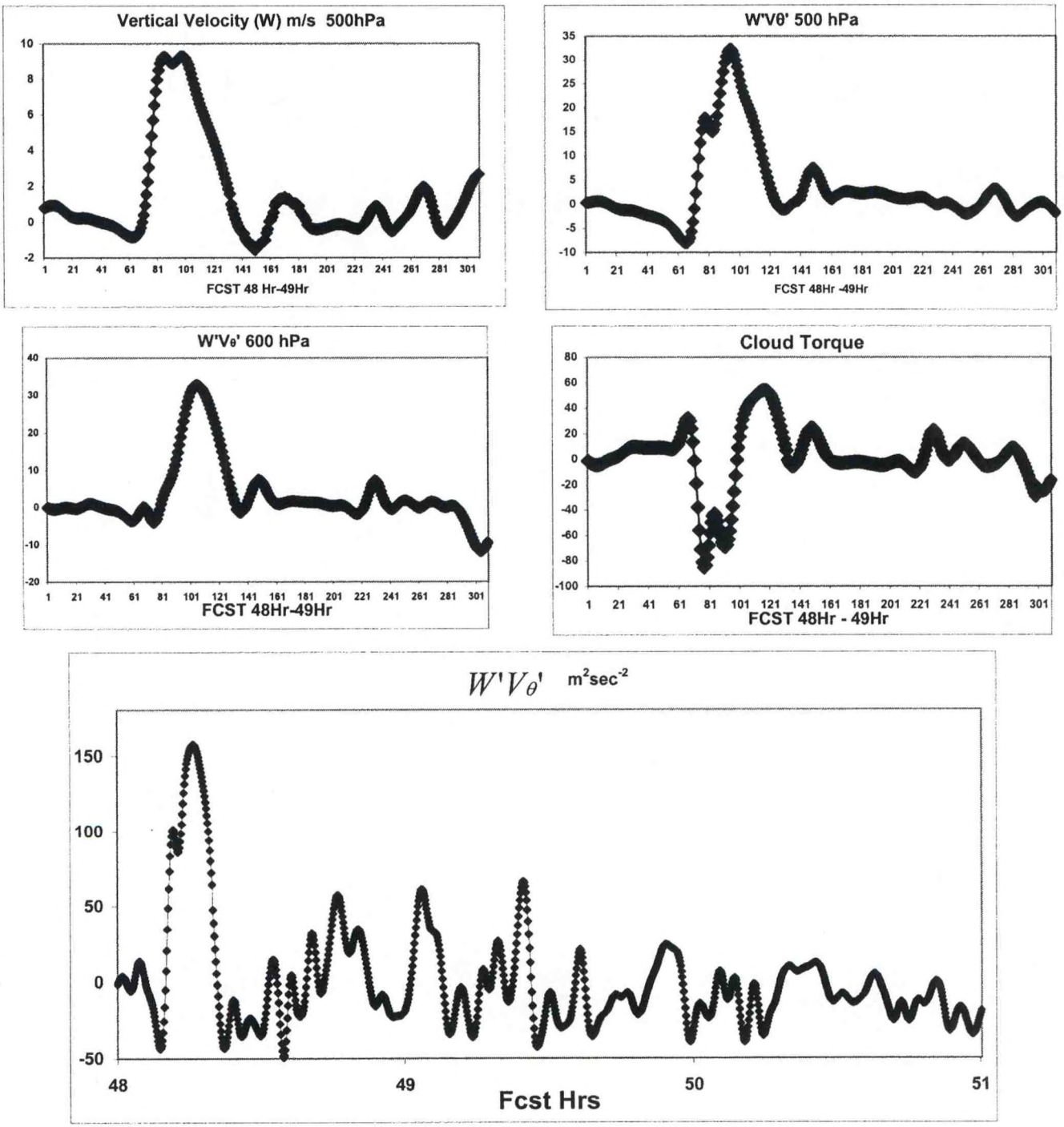

Fig. 10. (a) Vertical velocity (ms^{-1}) at 500 hPa, (b) vertical eddy flux of momentum (units) at 500 hPa, (c) vertical eddy flux of momentum at 600 hPa, (d) cloud torque (units) during every time step of a one-hour forecast between 48th and 49th hour of model integration. (e) is same as (c) but for a longer duration from 48th to 51st hour of integration.

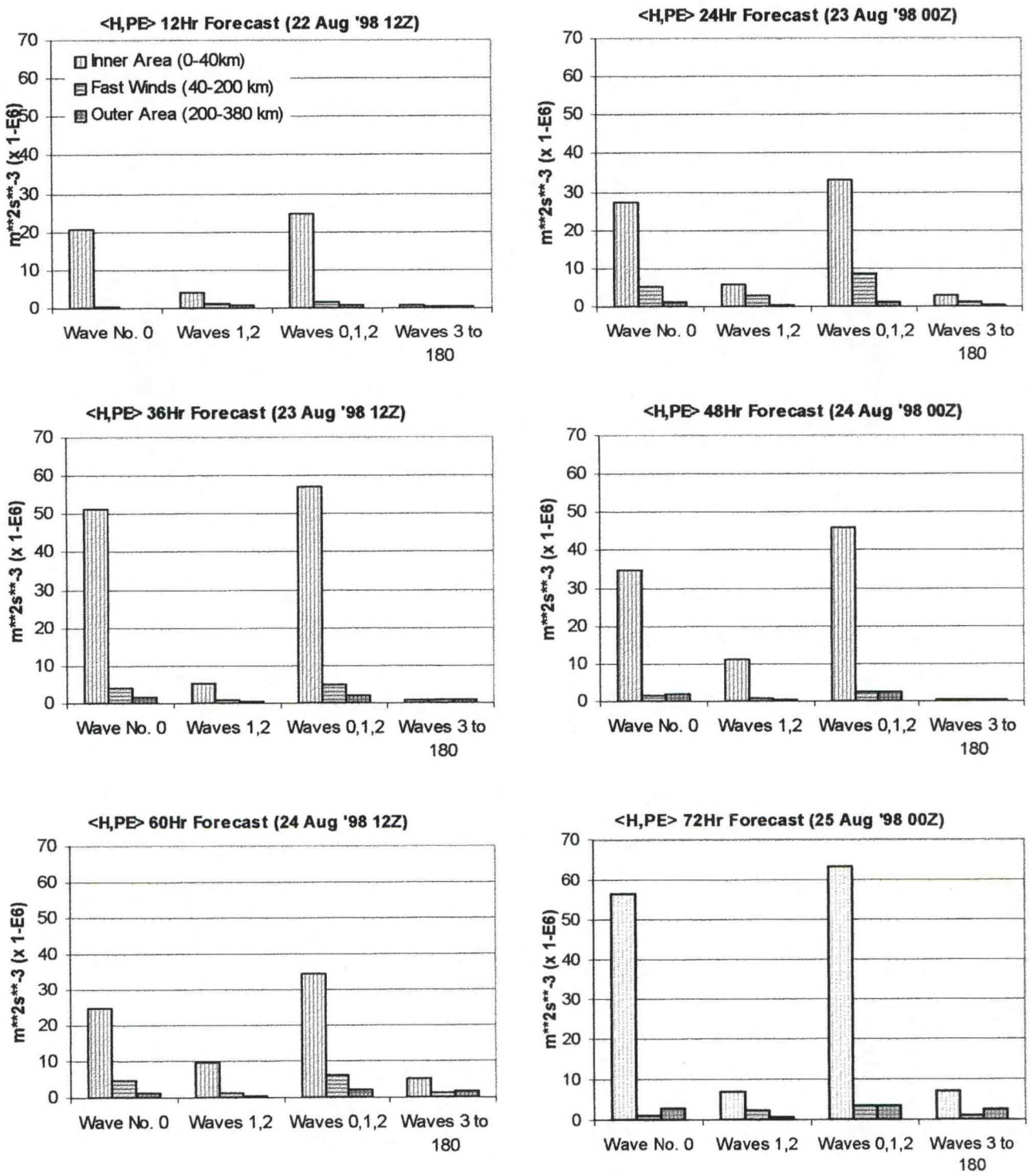

Fig. 11: Generation of available potential energy for Hurricane Bonnie. Three different histograms in each panel represent three regions – inner area (0-40 km), fast winds (40-200 km) and outer area (200-380 km). The panels from top to bottom are at different forecast times (a) 12 hr, (b) 24 hr, (c) 36 hr, (d) 48 hr, (e) 60 hr and (f) 72 hr of the model output.

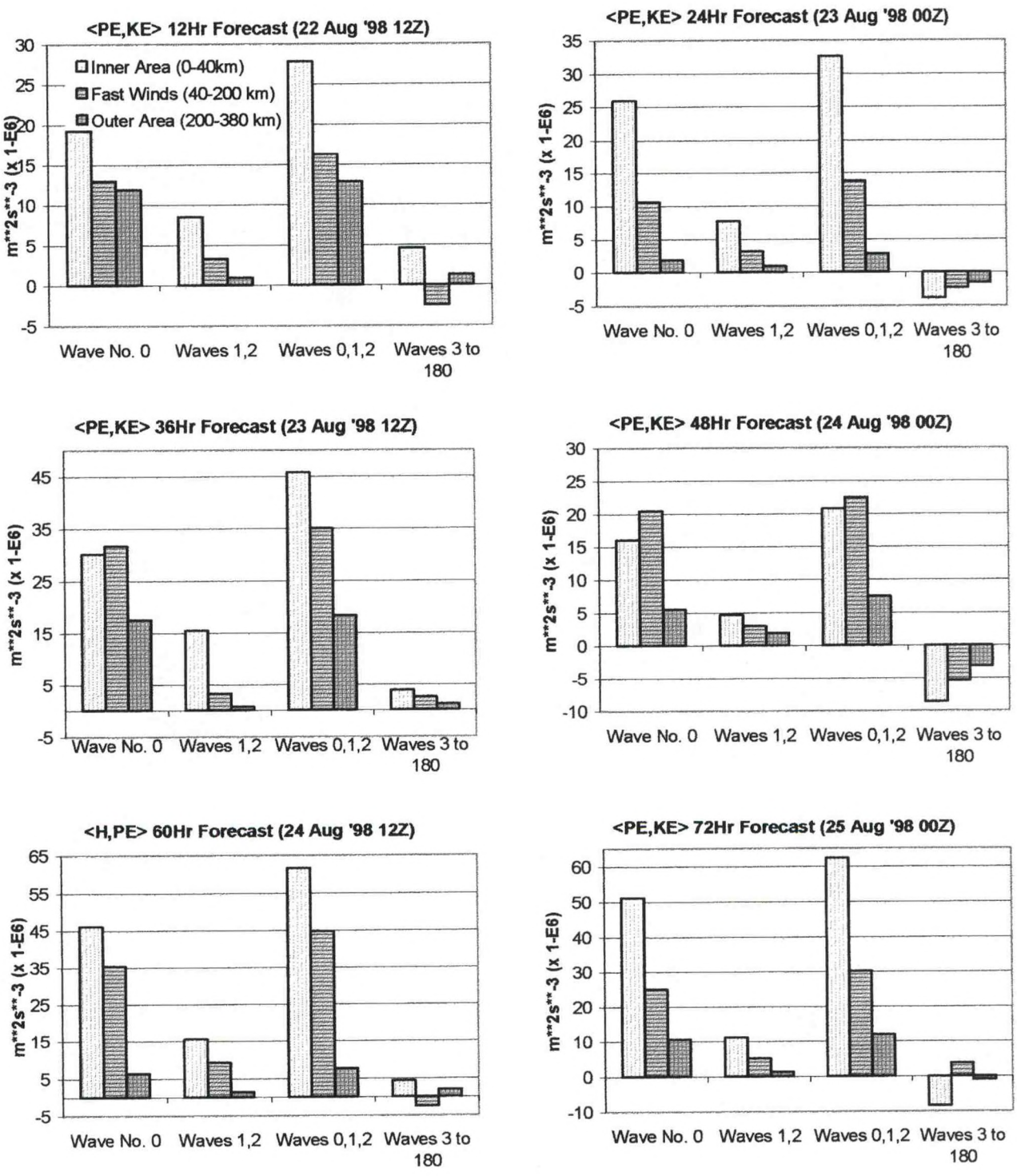

Fig. 12: Generation of Kinetic Energy by vertical overturning for Hurricane Bonnie. Three different histograms in each panel represent three regions – inner area (0-40 km), fast winds (40-200 km) and outer area (200-380 km). The panels from top to bottom are at different forecast times (a) 12 hr, (b) 24 hr, (c) 36 hr, (d) 48 hr, (e) 60 hr and (f) 72 hr of the model output.

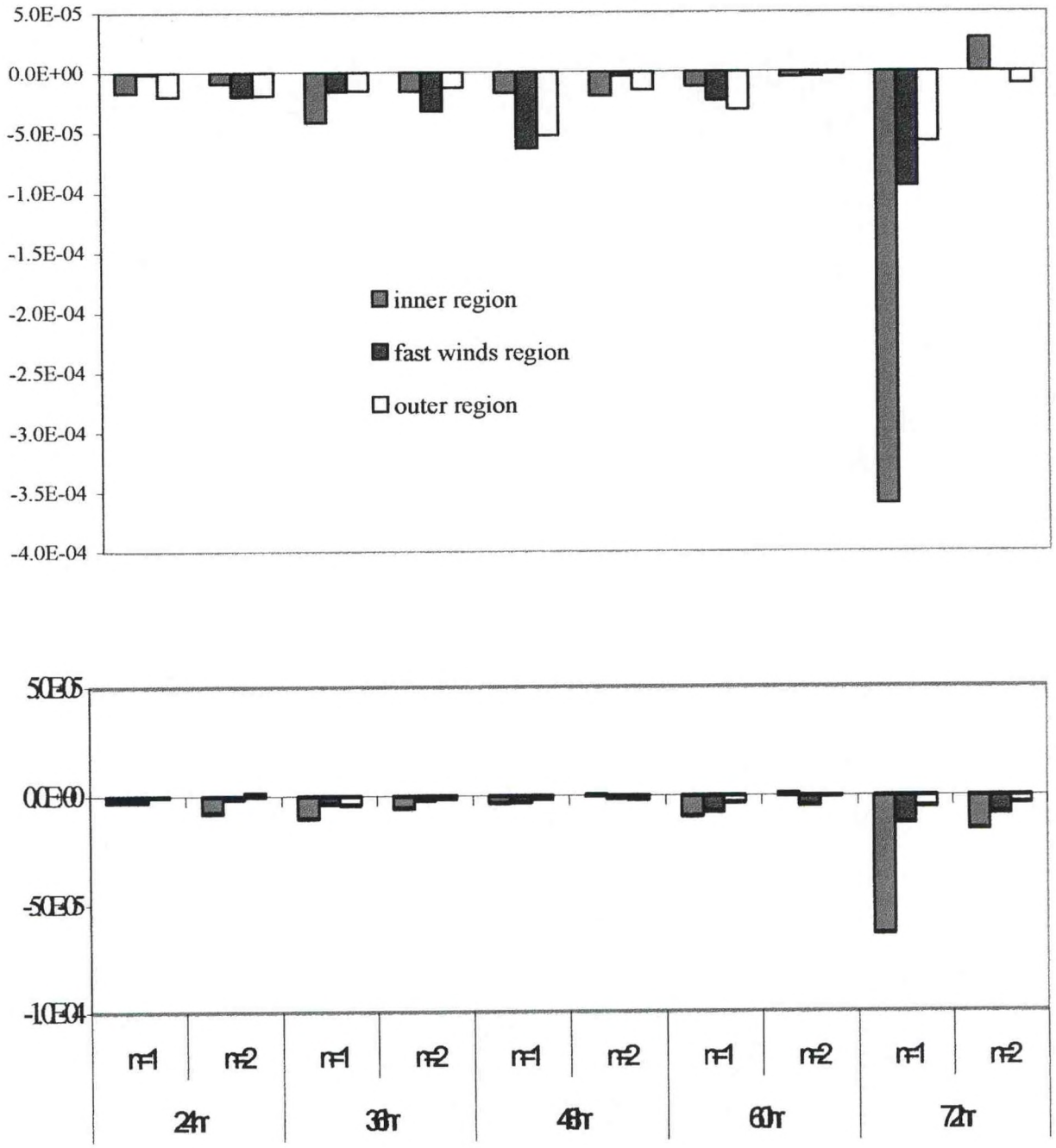

Fig. 13. Rate of change of (a) kinetic and (b) potential energy of wave numbers n=1 and n=2 due to interactions with pairs of waves with wave numbers (l,m) >2. Units are 10^{-5} m^2s^{-3}. The forecast hour is indicated along the abscissa.

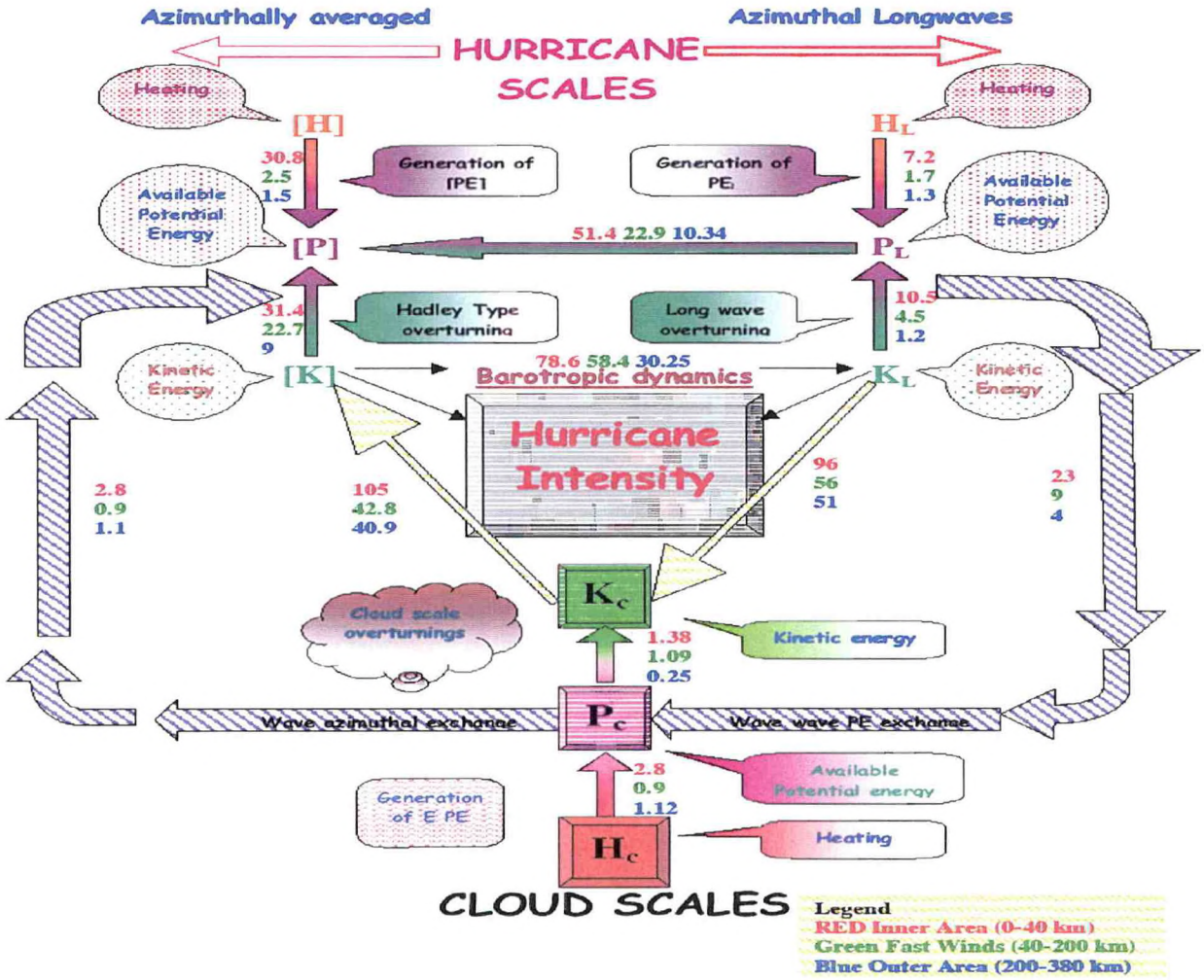

Fig. 14. Summary of energy exchange computations resulting in the final intensity of Hurricane Bonnie. Different colors in the numbers represent three different regions of computations (Red for inner area between 0 and 40 km, Green for fast wind region between 40 and 200 km and Blue for outer area between 200 and 380 km of radius). Arrow marks indicate the direction of energy exchange.

Table 1. List of Acronyms

MM5	5th Generation NCAR-PSU Meso-Scale Model
NCAR	National Center for Atmospheric Research
PSU	Pennsylvania State University
ECMWF	European Centre for Medium Range Weather Forecasts
CAMEX	Convection and Moisture Experiment
NASA	National Aeronautics and Space Administration
NOAA	National Oceanic and Atmospheric Administration
LASE	LIDAR Atmospheric Sensing Experiment
UTC	Universal Time Constant
FSU	Florida State University
TRMM	Tropical Rainfall Measuring Mission
DMSP	Defense Meteorological Satellite Program
PBL	Planetary Boundary Layer
MRF	Medium Range Forecasting

Table 2. Values of different torques along the path of the 3-D trajectory of wind maximum at 850 hPa for Hurricane Bonnie.

Fcst Hrs	00	12	24	36	48	60	72
Position of Vmax at 850 hPa	-68.3272 20.7498	-69.953 22.5838	-68.9196 25.5663	-70.8142 25.1711	-71.3739 26.6084	-72.3642 27.6505	-72.1295 29.4832
Pressure of the Parcel (hPa)	336	300	376	726	837	861	850
Pressure Torque $*10^{-4}$	.0214	-.0571	-.0741	-.0116	-.0063	-.0045	-.0022
Angular Momentum $*10^{-4}$	1.1630	1.1374	.9722	.7471	.6043	.4213	.2282
$\Delta M *10^{-4}$		-.0256	-.1652	-.2251	-.1428	-.1830	-.1931
Frictional Torque $*10^{-4}$	.0004	.0008	.0008	.0005	.0012	.0025	.0034
Cloud Torque $*10^{-4}$		.0474	.1089	.1317	.1895	.1779	.1911